EXPLORING THE ELECTRONIC AND MAGNETIC CHARACTERISTICS OF LITHIATED HOLEY Mo_8S_{12}: A STUDY IN INORGANIC CHEMISTRY

A Thesis Submitted to
the Graduate School of Engineering and Sciences of
İzmir Institute of Technology
in Partial Fulfillment of the Requirements for the Degree of

MASTER OF SCIENCE

in Chemistry

by
Fırat TAN

October 2023
İZMİR

We approve the thesis of **Fırat TAN**

Assist. Prof. Dr. Onur BÜYÜKÇAKIR
Department of Chemistry, İzmir Institute of Technology

Prof. Dr. Hasan ŞAHİN
Department of Photonics, İzmir Institute of Technology

Assoc. Prof. Dr. Mehmet YAĞMURCUKARDEŞ
Department of Photonics, İzmir Institute of Technology

Assist. Prof. Dr. Arzu UYAR
Department of Bioengineering, İzmir Institute of Technology

Assoc. Prof. Dr. Ümit AKINCI
Department of Physics, Dokuz Eylül University

4 October 2023

Asst. Prof. Dr. Onur Büyükçakır
Supervisor, Department of Chemistry
İzmir Institute of Technology

Prof. Dr. Hasan Şahin
Co-Supervisor, Department of Photonics
İzmir Institute of Technology

Prof. Dr. Gülşah ŞANLI-MOHAMED
Head of the Department of
Chemistry

Prof. Dr. Mehtap EANES
Dean of the Graduate School of
Engineering and Sciences

ACKNOWLEDGMENTS

I would like to thank Prof. Dr. Hasan Şahin and Assoc. Prof. Dr. Mehmet Yağmurcukardeş, who taught me work discipline, time management and being a good team-mate throughout my undergraduate and graduate education. At the same time, I would like to express my gratitude to Assist. Prof. Dr. Onur Büyükçakır for his academic support in all aspects.

Thank you to Yankı Yayak, Yiğit Sözen, Mehmet Başkurt, Tuna Duran, Ali Cem Demirok, Anılcan Kuş, and Ozan Orhan of the CENT group; it was a pleasure and a great learning experience working with you.

I like to express my gratitude to my family, who have been supporting me at every moment of my life, my team-mates, and coaches from the IYTE volleyball team, and my friends who have supported me a lot: Ebru Ada, Mert Kurak, Emre Yıldırım, Deniz Güngen, Şule Bektaş, and Merve Aydın.

Finally, and most importantly, I would like to give special thanks to Meryem Alkan for her support, love, and patience.

ABSTRACT

EXPLORING THE ELECTRONIC AND MAGNETIC CHARACTERISTICS OF LITHIATED HOLEY Mo_8S_{12}: A STUDY IN INORGANIC CHEMISTRY

Since graphene, the ultra-thin carbon compound, gained popularity with its remarkable electrical capabilities, various two-dimensional (2D) van der Waals-type materials have come into focus. Investigation of the electrical and optical properties of materials at atomic scale is required to understand the unique electronic behavior brought on by quantum size effects. The development of optoelectronic devices with novel features is facilitated by an increased understanding of the properties of matter within the context of theoretical techniques. This thesis includes the investigation of the lithiated holey Mo_8S_{12} structure through calculations based on density functional theory (DFT).

Motivated by the recent experimental realization of holey structure of transition metal dichalcogenides (TMDs), in this thesis, the holey structure of Mo_8S_{12} is investigated by means of DFT-based calculations. The geometry optimization and phonon band dispersion calculations show the structural and dynamical stability of free-standing holey single-layer Mo_8S_{12}. In addition, electronic band dispersions reveal the direct band gap semiconducting nature of the structure. In order to investigate the lithiation capacity of single-layer Mo_8S_{12}, effect of Li doping on the properties of Mo_8S_{12} is analyzed by considering both one- and double-sided lithiation. As one surface of single-layer Mo_8S_{12} is fully saturated with Li atoms, a dynamically stable half-metallic structure is formed. The corresponding electronic band structures reveals the metallic behavior of the two-side lithiated single-layer. Overall, tunable electronic properties of single-layer holey Mo_8S_{12} via lithiation makes it suitable candidate for various nanoelectronic applications, such as memories, capacitors, gate insulators, energy storage, high-frequency modulation in communication devices.

ÖZET

LİTYUMLANMIŞ DELİKLİ Mo_8S_{12}'NİN ELEKTRONİK VE MANYETİK ÖZELLİKLERİNİN ARAŞTIRILMASI: ANORGANİK KİMYA ÇALIŞMASI

En küçük karbon bileşiği olan grafen, eşsiz elektriksel özellikleriyle popülerlik kazandığından beri, çeşitli iki boyutlu (2B) van der Waals tipi malzemeler ilgi odağı haline geldi. Malzemelerin elektriksel ve optik özelliklerinin atomik ölçekte araştırılması, kuantum boyutu etkilerinin getirdiği benzersiz elektronik davranışı anlamak için gereklidir. Yeni özelliklere sahip optoelektronik cihazların geliştirilmesi, teorik teknikler bağlamında maddenin bu özelliklerinin daha iyi anlaşılmasını kolaylaştırmıştır. Bu tez, yoğunluk fonksiyonel teorisine (DFT) dayalı hesaplamalar yoluyla lityumlanmış delikli Mo_8S_{12} yapısının incelenmesini içerir.

Geçiş metali dikalkojenitlerin (TMDs) delikli yapısının yakın zamanda deneysel olarak gerçekleştirilmesinden motive edilen bu tezde, Mo_8S_{12}'nin delikli yapısı yoğunluk fonksiyonel teorisine dayalı olarak araştırılmaktadır. Geometri optimizasyonu ve fonon bandı dağılım hesaplamaları, serbest duran delikli tek katmanlı Mo_8S_{12}'nin yapısal ve dinamik kararlılığını göstermektedir. Ek olarak, elektronik bant dağılımları, yapının doğrudan bant aralığı yarı iletken doğasını ortaya koymaktadır. Tek katmanlı Mo_8S_{12}'nin litiasyon kapasitesini araştırmak için, Li katkısının Mo_8S_{12}'nin özellikleri üzerindeki etkisi, hem tek hem de çift taraflı litiasyon dikkate alınarak analiz edilir. Tek katmanlı Mo_8S_{12}'nin bir yüzeyi tamamen Li atomları ile doyurulduğundan, dinamik olarak kararlı bir yarı metalik yapı oluşur. Karşılık gelen elektronika bant yapıları, iki taraflı taşlanmış tek katmanın metalik davranışını ortaya koyuyor. Genel olarak, tek katmanlı delikli Mo_8S_{12}'nin lityumlama yoluyla ayarlanabilir elektronik özellikleri, onu bellekler, kapasitörler, kapı (gate) izolatörleri, enerji depolama, iletişim cihazlarında yüksek frekanslı modülasyon gibi çeşitli nanoelektronik uygulamalar için uygun aday yapar.

TABLE OF CONTENTS

LIST OF FIGURES vii

LIST OF TABLES ix

CHAPTER 1. INTRODUCTION 1

CHAPTER 2. THEORETICAL BACKGROUND AND METHODOLOGY 7
2.1. Thomas-Fermi Approximation 8
2.2. Density Functional Theory 8
2.2.1. Hohenberg-Khon Theorems 9
2.2.2. Kohn-Sham Equations 10
2.2.2.1. Exchange-Correlation Functionals 12
2.2.3. Hellman-Feynman Theorem 13
2.2.4. Hybrid Functionals 13
2.3. Computing Phonons 14
2.4. Computational Parameters 16

CHAPTER 3. LITHIATED SINGLE-LAYER HOLEY MO_8S_{12}: ELECTRONIC, MAGNETIC AND VIBRATIONAL CHARACTERISTICS 17
3.1. Single-Layer Mo_8S_{12} 18
3.2. Interaction of Single-Layer Mo_8S_{12} with Single Lithium Atom 20
3.3. One-Sided Lithiation 23
3.4. Double-Sided Lithiation 24
3.5. Conclusion 25

CHAPTER 4. OVERALL DISCUSSION 26

REFERENCES 27

LIST OF FIGURES

Figure **Page**

Figure 1.1. Structure and classification of different 2D materials. 3

Figure 1.2. The atomic structure of W_8Se_{12}. (a) ADF-STEM images of the W_8Se_{12} structure formed in the single-layer WSe_2. The wight dash box is enlarged in panel (b). The corresponding fast Fourier transform (FFT) pattern of the whole image. (b-d) ADF-STEM images, simulated images, and an atomic model of the W_8Se_{12} phase, respectively. The dash boxes indicate the unit cell. (e) Intensity line profiles for the dashed line in panels (b) and (c). Blue spectra correspond to experimental ADF-STEM images and red ones for the simulated image. 6

Figure 2.1. Density functional theory approach to a many-body system. Arrows (left) represents the corresponding interactions between electrons and the nuclei. 9

Figure 2.2. Schematic representation of the self-consistency cycle in Kohn-Sham DFT calculations. The arrow pointing back to the start of the cycle is a pictorial representation of the energy and force convergence criteria implemented in first principle calculations. The three dots in the fourth and sixth boxes indicate there are numerous terms that would not fit within the size of the box. 11

Figure 3.1. For the single-layer of Mo_8S_{12}: (a) Top and side views of the crystal structure. (b) The simulated STM image and (c) the phonon band structure. (d) The electronic band structure and corresponding partial density of states (PDOS). PDOS are normalized to unity in order to show the contribution of individual atoms. 18

Figure 3.2. Top and side views of Li adsorption on Mo_8S_{12} for (a) various sites which are marked by red circles and (b) the energetically most stable structure. (c) The PDOS corresponding to Li adsorption in the Mo-Mo bridge side. PDOS are normalized to unity for the sake of clarity. 21

Figure 3.3. (a) Top view of single-layer Mo_8S_{12} describing three different diffusion paths for single Li atom. (b-d) Energy barrier profiles of Li adatom on single-layer Mo_8S_{12} through different paths. 22

Figure 3.4. For the one-side lithiated single-layer of Mo_8S_{12}; (a) Top and side views of magnetization charge density at the isosurface value of 5×10^{-3}e Å^{-3}. (b) The phonon band structure. (c) The electronic band structure and the normalized PDOS. Solid blue and dashed red lines stand for opposite spin states, respectively. 24
Figure 3.5. For the double-side lithiated single-layer of Mo_8S_{12}; (a) Top and side views of the crystal structure. (b) The phonon band structure and (c) the electronic band structure with normalized PDOS of the individual atoms. 25

LIST OF TABLES

Table **Page**

Table 3.1. For the bare and lithiated single-layer of Mo_8S_{12}; optimized in-plane lattice parameters (a=b), thickness (t), the work function for the two surfaces (ϕ_{Li} and ϕ_{S}), calculated cohesive energy per atom (E_{Coh}), the amount of charge transfer from Li to Mo_8S_{12} ($\Delta\rho$), and electronic band gap calculated with GGA functionals (E_{Gap}), half-metallic (HM) behaviour of the one-side lithiated Mo_8S_{12} and metallic (M) behaviour of the double-side lithiated Mo_8S_{12}. 19

Table 3.2. For the adsorption of single Li atom on single-layer Mo_8S_{12}; adsorption positions of Li before and after the structural relaxations. The corresponding binding energies, E_b; and the amount of charge donated by Li atom to Mo_8S_{12} layer, ρ. 20

CHAPTER 1

INTRODUCTION

The rapid development of nanotechnology in the last years makes the need for new materials irreplaceable. Ultra-thin materials are important for this and 2D materials have drawn great interest owing to their potential for various applications such as sensors[9], supercapacitors[26], lithium-ion batteries (LIBs)[85] and separation membranes[15]. In order to meet the demand for LIBs, 2D materials have been widely studied owing to their cyclic stability, high-rate capability, and safety. Both theoretical and experimental studies have revealed the potential for LIBs applications of graphene[104,108,107,126], silicene[27,113,103,114] and recently TMDs[117,40,12].

TMDs are promising options for optoelectronic devices as well as inexpensive catalysts for energy production[111,42]. TMDs are defined by the formula MX_2, where M represents a transition metal and X denotes chalcogen, and in the crystal structures of TMDs, there exist three-layered covalent bonds of X-M-X[16]. The majority of atomically thin TMDs show unusual characteristics compared to their bulk counterparts due to the anisotropic nature of bonding[17,105,99]. Exfoliation techniques, both mechanical and chemical, have been developed and are often used in laboratories to exfoliate bulk structures into their individual layers[68]. However, it is essential to develop synthesis techniques that provide accurate morphological control for applications as well as uniform, scalable 2D films[65]. There have been investigations on vertically grown 2D TMDs, which have high surface energy, metastable edge sites, and potential for catalysis and hydrogen evolution reactions[50,58,109,119].

Among TMDs, molybdenum disulfide (MoS_2) stands out as the most extensively studied 2D layered material, characterized by its graphene-like structure. In the S-Mo-S layer, while the bonds between the Mo and S atoms are strong, the forces between the layers are limited to van der Waals (vdW), leading to strong intralayer and weak interlayer interactions. Thus, providing ease in exfoliation procedures. MoS_2 possesses a thickness-dependent band gap, varying from an indirect band gap of approximately 1.29 eV in the bulk form of the structure to a direct band gap of about 1.89 eV in single-layer form[96,61,25]. MoS_2 demonstrates intense photoluminescence (PL), high in-plane carrier mobility, and robust mechanical properties. Additionally, few-layer MoS_2-based materials have gained significant prominence in practical applications due to their strong interaction with light and

the quantum confinement-induced transition from an indirect to a direct band gap. Field-effect transistors, photodetectors, light-emitting diodes, solar cells, spintronics, and many environmental technologies are among the areas of use of MoS_2 [28,10,8,66,122,78,129,116,123].

The 2H and 3R phases of MoS_2 are the most stable and frequently found in nature. Both of these phases have trigonal prismatic coordination of molybdenum atoms, differing primarily in their stacking order[44,20,124,95]. Conversely, the 1T phase represents a metastable state, featuring octahedral coordination of molybdenum atoms and a different stacking order compared to the other two phases[21]. Previously reported methods for the synthesis of metastable phases of MoS_2 include chemical exfoliation. This method utilizes lithium atoms to intercalate between material layers with the use of various surfactants such as n-butyllithium (n-BuLi)[81]. Also, liquid phase exfoliation (LPE) stands out as a promising technique for large-scale production of 2D-MoS_2 nanosheets due to its versatility and straightforward operation. The basic principle of LPE is based on deactivating the weak vdW interactions between nanosheets with ultrasonic sound waves. Both theoretical studies and experiments have confirmed the significant role of selecting a suitable solvent in LPE to ensure successful and sufficient exfoliation, considering the hydrophobic nature of layered materials[43,92]. However, the solvents typically used for LPE are usually toxic, have high boiling points, are hard to remove, reduce performance in applications, and cause significant environmental risks[94,30]. Mechanical exfoliation, another method used to separate bulk MoS_2 layer by layer, is one of the top-down methods that is very convenient and simple compared to any epitaxial synthesis. This method is reliable enough to represent the characteristics of the added material. Bulk MoS_2 is reduced to the nanoscale through a process involving adhesive tape[55,70]. The exfoliation procedure is repeated approximately 60-70 times, or for ten minutes per sample. Afterwards, mechanically exfoliated MoS_2 is affixed to a quartz substrate, with this process repeated up to ten times[2]. Additionally, chemical vapor deposition (CVD) is another common method utilized to produce MoS_2 monolayers of different phases[72]. CVD is used to synthesize the MoS_2 layer on Si/SiO_2 substrates by utilizing MoO_3 and S powders as reactants[57].

The mechanical properties of MoS_2 nanotubes and the impacts of strain on MoS_2 band structure and carrier effective masses were investigated by Li et al.[62]. The band gap and carrier effective masses are sensitive to the strain and thus modifiable under uniaxial strain. Due to their tunable direct band gap, zigzag nanotubes have the potential to be utilized in optoelectronics. However, despite having an indirect band gap, armchair nanotubes can undergo a semiconductor-to-metal transition at a critical tensile strain of 8%, which has the potential to be used in nanodevices like electronic switches and strain

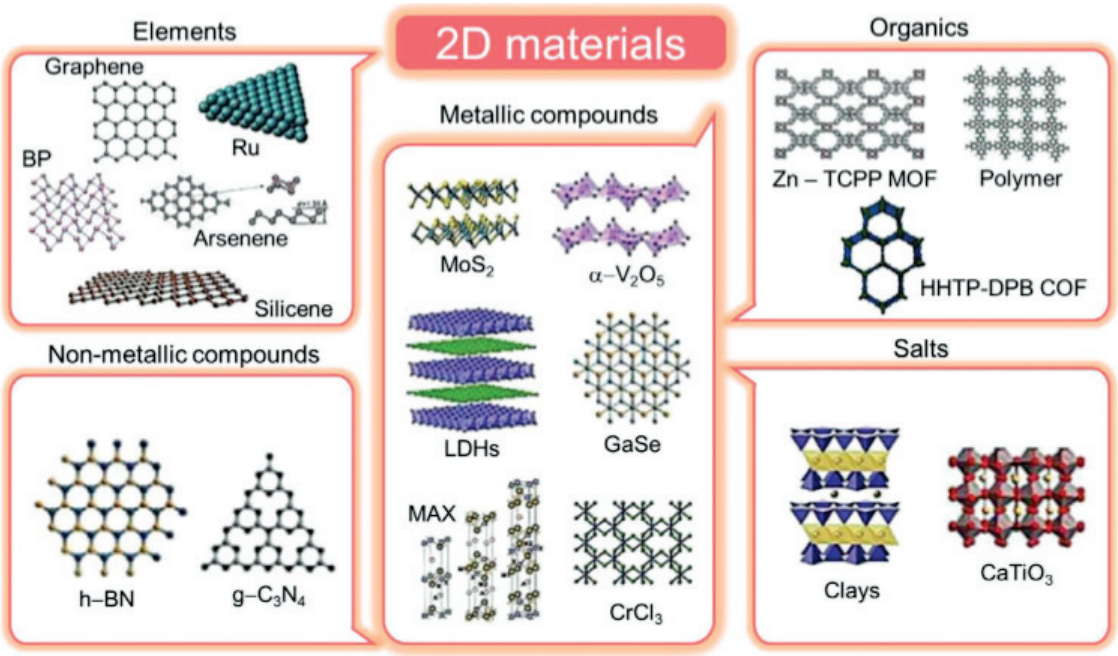

Figure 1.1. Structure and classification of different 2D materials.

sensors. Holes consistently have larger effective masses than electrons in MoS_2 nanotubes in both armchair and zigzag configurations and are more susceptible to external strain. Piezoelectric nanogenerators (PNGs) based on 2D MoS_2 shells were reported by Han et al., and the authors were successfully able to control particle sizes by varying the size of the polystyrene (PS) used[33]. The polarity and piezoelectricity of the PNGs based on the MoS_2 shells were validated as PNG features. About 0.3 kPa of pressure was required to generate the output voltage. Additionally, the output voltage of 1.2 V was obtained at 4.2 kPa of pressure. The increase and decline were non-linear with respect to the magnitude of force in the case of 1 μm MoS_2 shell film, and a hysteresis characteristic was noticed below 4 kPa of pressure. For the shells with widths of 1 μm, in particular, high-power production characteristics and non-linear hysteresis behavior were noted. The production of 2D MoS_2 flakes with various number of layers using a pulsed Ar-flow aided CVD technique, using Mo foil and S powder as precursors, has been verified by Chen et al.[14]. On the basis of variations in Mo/S concentration under various pulsed Ar-flow on-times, a potential growth mechanism for the thickness evolution of MoS_2 flakes is presented. Apart from these, changes in electronic, optical, and magnetic properties as a result of strain applied to 2D MoS_2 have been investigated in many studies[45,120,19,11,67,74,60,88,93].

Elements, metallic and non-metallic compounds, organics, and salts shown in Fig. 1.1 belong to the class of 2D materials[91]. Hexagonal boron nitride (h-BN) is an analog of graphene with a crystallographic appearance containing boron and nitrogen atoms

instead of carbons. h-BN has unique electronic properties such as wide band gap, low dielectric constant, chemical inertness, and high thermal conductivity. Bulk h-BN, which has atomically smooth and sp^2 hybridized surface of covalent bonds similar to graphene, which attracted tremendous attention as a great substrate for graphene. 2D h-BN in the form of few-layer crystals or monolayers has emerged as a fundamental building block for vdW heterostructures[31]. The synthesis of 2D crystals and associated heterostructures has advanced significantly, but nothing has been done to address the nucleation and growth fundamentals that control the morphology that results from synthesis. Atoms near the borders of the basal plane have higher free energy as favored nucleation sites. However, atoms on the basal plane do not have dangling bonds and are not chemically active. Sheets tend to grow laterally into single-layer structures during the synthesis process[50]. Additionally, in the case of MoS_2, it has been suggested that having a low Mo precursor partial pressure (P_{Mo}) is helpful for consistently growing single-layer MoS_2 thin films over an extensive area[47,64]. In some cases, the fast sulfurization of metal-seeded substrates results in the growth of MoS_2 nanosheets that are vertically stacked on the substrate. This is caused by a decrease in the elastic strain energy that occurs during the horizontal growth of MoS_2 nanosheets[46].

Several methods have been developed in the last decade to produce single- or few-layered graphene sheets[128,127]. The process of mechanical exfoliation, often known as the Scotch tape method, generates sheets of the highest quality and has a very low defect density. As it only provides a few sheets on supported substrates, this method is not scalable. The most scalable technique for uses such as composites and energy storage are the oxidation and exfoliation of graphite to produce graphene oxide (GO), which can then be reduced by restoring it to its graphitic structure[97]. The resulting form of graphene, known as reduced graphene oxide (rGO), has defects but can be produced in laboratories frequently in gram amounts and has recently been industrialized to ton quantities[83]. Other industrialized techniques, such CVD growth[63] and LPE of graphite[36], have produced graphene materials with high quality and amounts between the two extremes and provide exact combinations of properties required for various applications[90]. While graphene sheets produced by many other processes always have defects in nanoscale, mechanically exfoliated graphene sheets are frequently of high atomic order. The presence of defects in graphene sheets appears to be undesirable since defects have the potential to adversely affect the mechanical and electrical conductivity properties of it. However, defects in the structure at nanoscale provide unique physical and chemical characteristics to nano-sized materials as a result of quantum confinement effects, providing qualities that are desired

for particular applications[89,13,101]. For instance, the presence of defects may make it easier for functional groups to attach and may affect other properties such as interactions with other materials like polymer or biological agents[24].

Holey graphene (HG) is a graphitic material which contains numerous mesopores that is mainly advantageous for ion longitudinal transport and conductive skeletons for electron transfer. Pore sizes range from nm to microns and can be produced using a variety of methods and procedures. There are multi-layered graphene structures with arbitrarily distributed pores on their basal planes. When HG sheets are combined to produce a 3D porous material, it is referred to as porous graphene[100,106]. In graphene sheets without pores, any ion or molecule possesses two degrees of freedom. Conversely, in the HG material, ions and molecules exhibit three degrees of freedom owing to the presence of interlayer access through pores. Another feature of holey graphene is the lack of continuous C atoms that weaken interlayer attractive forces, i.e., the van der Waals interactions between the layers. The C atoms between the layers appear in the increasing interlayer space between the sheets. The presence of a high number of pores and more interlayer distance enhances ion mobility and mass transfer, thus providing significant opportunities for porous graphene in water filtration and desalination[118,98,18]. Among the several possible morphological alterations, hollow and graphitic carbon nitride (g-C_3N_4) nanotubes attract attention due to their ability to support charge carrier movement through the 1D length and thus improve successful carrier separation. Nanotubes also improve incoming light absorption, while the accessible inner and outer surfaces provide a higher specific surface area and hence more catalytic active sites for photo-reactions[121]. Other research reveals that porous g-C_3N_4 nanosheets outperform pristine nanosheets in photo-catalytic effectiveness due to their higher surface area and many channels that allow mass diffusion[82]. To improve the photo-catalytic performance of porous g-C_3N_4 nanotubes, the designed model should be near-ideal. To date, a number of methods for synthesis of g-C_3N_4 nanotubes have been proposed. The utilization of hazardous chemicals, severe reaction conditions, high expenses, synthetic intricacies, and a lack of scalability are among the drawbacks encountered in previously published studies[59,112,29].

Apart from widely studied 2D TMDs materials, such as MoS_2 and WS_2, novel holey phase of W-based chalcogenides, namely W_8Se_{12}, has been recently demonstrated (See Fig. 1.2). Single-layer form of W_8Se_{12} was reported to be an integrated phase controllably created in a single-layer WSe_2. It was also reported that single-layers of W_8S_{12}, W_8Se_{12}, Mo_8S_{12}, and Mo_8Se_{12} were also predicted to possess direct band gap with outstanding anisotropic optical absorption in the visible spectrum[75]. Furthermore, under

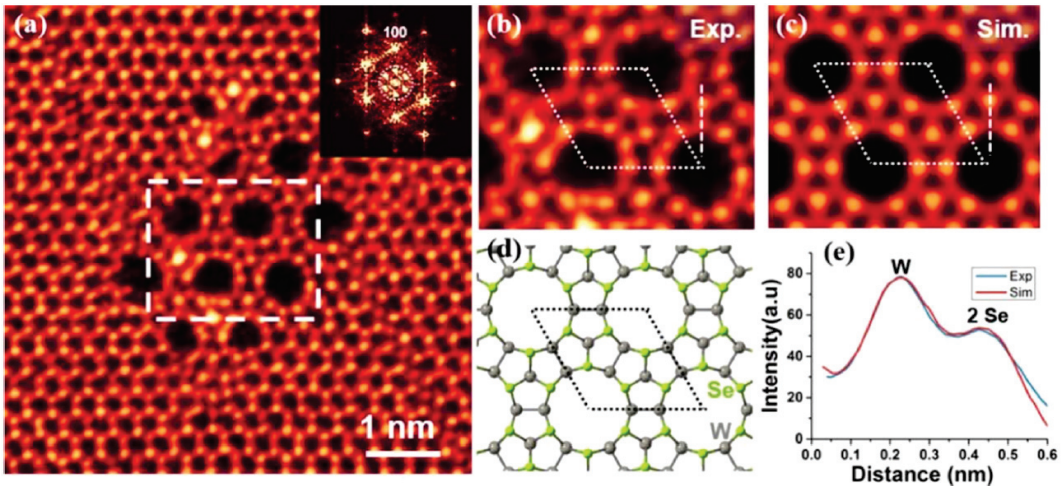

Figure 1.2. The atomic structure of W_8Se_{12}. (a) ADF-STEM images of the W_8Se_{12} structure formed in the single-layer WSe_2. The wight dash box is enlarged in panel (b). The corresponding fast Fourier transform (FFT) pattern of the whole image. (b-d) ADF-STEM images, simulated images, and an atomic model of the W_8Se_{12} phase, respectively. The dash boxes indicate the unit cell. (e) Intensity line profiles for the dashed line in panels (b) and (c). Blue spectra correspond to experimental ADF-STEM images and red ones for the simulated image.

uniaxial strain, direct-indirect-metal transitions were investigated for single-layer W_8Se_{12}.

In this thesis, the structural, electronic, and vibrational characteristics of lithiated and two-dimensional ultra-thin Mo_8S_{12} using ab initio calculations. Calculations of the phonon band distribution and total energy optimizations showed that the free-standing Mo_8S_{12} layer was structurally and dynamically stable. It was also demonstrated that one-sided lithiation can transform the non-magnetic semiconductor Mo_8S_{12} to a ferro-magnetic half-metal, and that lithiation from both surfaces can result in a transition from semiconductor to metal.

CHAPTER 2

THEORETICAL BACKGROUND AND METHODOLOGY

As systems get smaller, the laws of quantum mechanics operate rather than Newton's laws. Solving the Schrödinger equation reveals properties inherent in the wave functions of such systems, ψ,

$$\hat{H}\psi_i = E_i\psi_i \tag{2.1}$$

where E_i denotes the energy eigenvalue of that quantum state, ψ_i indicates the wave function of the energy eigenvalue, and $\hat{H}$ refers an energy operator known as the Hamiltonian operator. The Hamiltonian of a system contains terms for all potential and kinetic interactions between electrons and nuclei. The Hamiltonian operator when all the terms are added is,

$$\begin{aligned}\hat{H} = &\frac{\hbar}{2m_e}\sum_i \nabla_i^2 - \frac{1}{4\pi\varepsilon_0}\sum_{i,A}\frac{Z_A e^2}{\mid r_i - R_A \mid} + \frac{1}{2}\frac{1}{4\pi\varepsilon_0}\sum_{i\neq j}\frac{e^2}{\mid r_i - r_j \mid} \\ &- \sum_A \frac{\hbar^2}{2M_A}\nabla_A^2 + \frac{1}{2}\frac{1}{4\pi\varepsilon_0}\sum_{A\neq B}\frac{Z_A Z_B e^2}{R_A - R_B},\end{aligned} \tag{2.2}$$

where m_e stands for the electron mass, e stands for the electron charge, $\hbar$ is the Planck constant, and 1/4 π ε_0 is the Coulomb constant. i and j indices stand for electrons. Z_A and Z_B stand for nuclear charges. M_A and M_B are the masses of nuclei, r and R denote to the spatial coordinate of corresponding electron and atom, respectively. The kinetic energy of electrons and nuclei is discussed in the first and fourth terms, respectively. The potential energy operator is made up of the second, third, and final terms, which correspond to the electron-nucleus, electron-electron, and nucleus-nucleus interactions, respectively. It is simple to solve the Schrödinger equations for basic systems, such as hydrogen-like systems or single particles, because their Hamiltonians are devoid of the majority of interaction components. However, the environment becomes disordered when more particles interact. Solving the Schrödinger equation for systems with numerous electron-electron interactions is an extremely challenging task, leading to the application of various approximation methods.

2.1. Thomas-Fermi Approximation

The Thomas-Fermi is another approximation that operates under the assumption that the electrons' kinetic energy are considered a function of their electron density[23]. The equation is obtained by writing the kinetic energy term as a function of electron density;

$$T[n] = C_F \int n^{5/3}(r)dr \tag{2.3}$$

where n(r) is the electron density and C_F is the Fermi coefficient. The total energy of the system is made up of electron-nucleus and electron-electron interaction terms;

$$T[n] = C_F \int n^{5/3}(r)dr - Z \int \frac{n(r)}{r}dr + \frac{1}{2}\int\int \frac{n(r_1)n(r_2)dr_1dr_2}{\mid r_1 - r_2 \mid} \tag{2.4}$$

Reducing Eq. 2.4 results in the system's ground state energy;

$$N = \int n(r)d^3r \tag{2.5}$$

The efficiency of including electron density rather than interacting electrons is demonstrated by the Thomas-Fermi model, which simplifies the system in terms of electron density but excludes the exchange and correlation effects. The density functional theory depends on this concept.

2.2. Density Functional Theory

DFT, a very popular model of computational quantum mechanics since the 1970s, provides a first-principle method for solving the Schrödinger equation of many-body systems. However, until the 1990s, when the approximations used in the theory were considerably improved to better simulate the exchange and correlation interactions, DFT was not thought to be accurate enough for computations in quantum chemistry. Compared to more conventional approaches, such as exchange only Hartree-Fock (HF) theory and its descendants that take electron correlation into consideration, computational costs are quite low. It is frequently used for investigating at the various ground-state characteristics of

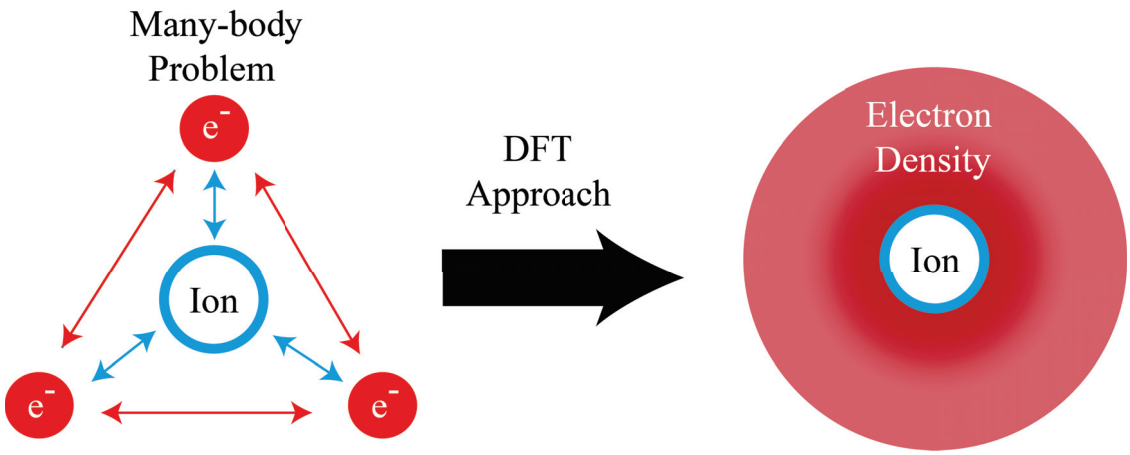

Figure 2.1. Density functional theory approach to a many-body system. Arrows (left) represents the corresponding interactions between electrons and the nuclei.

atoms, molecules, and condensed matter in chemistry, physics, and material science. DFT uses electron density functional that only depend on x, y, and z coordinates. It reduces the N electron many-body system of 3N spatial coordinates to 3 spatial coordinates. Because of this, DFT has a low cost and short calculation time, as well as good accuracy.

DFT still has problems accurately describing intermolecular interactions, particularly van der Waals forces, charge transfer excitations, transition states, global potential energy surfaces, dopant interactions, and some strongly correlated systems, as well as band gap and ferromagnetism calculations in semiconductors. The accuracy of DFT in the treatment of systems where dispersion is dominant or where dispersion competes considerably with other effects can suffer from the incomplete treatment of dispersion. Current research focuses on the development of novel DFT techniques in order to solve this problem by changing the functional or incorporating additive terms.

2.2.1. Hohenberg-Khon Theorems

Hohenberg and Kohn initiated the approach in 1964. They claim that the ground state of a many body system can be represented by the functional of electron density[39]. Two theories can be used to explain this supposition: (i) the external potential energy, V_{ext}, of a many-body system agrees with a functional of electron density, $n_{(r)}$, which is specific to the system. (ii) If the ground-state density is used as the input density, the electron density functional can be used to calculate the total energy of the system because it yields a global minimum energy value. The Hamiltonian's expectation value provides the ground-state energy,

$$E = < \psi_0 \mid H \mid \psi_0 >= T[n] + V_{int}[n] + E_{II} \int d^3 r V_{ext}(r) n(r)$$
$$T[n] + V_{int}[n] = F_{HK}[n], \tag{2.6}$$

where E_{II} refers to the nuclei-nuclei interaction, V_{int} represents the energy of electron-electron interactions, and T[n] indicates that the kinetic energy of electrons. The constant F_{HK}[n] refers to the sum of the kinetic energy of electrons.

2.2.2. Kohn-Sham Equations

In order to reduce the functional energy, Kohn-Sham suggested a method based on the Hohenberg-Kohn theorems in which the charge density is distributed across all densities containing N electrons. The system can be represented as a many-body system with non-interacting electrons[49]. While the exchange-correlation functional E_{xc}[n] is used to account for the electron-electron interactions, the ground-state electron density is obtained from the solution of the Schrödinger equation of non-interacting terms. Consequently, the Kohn-Sham method's functional definition is as follows:

$$E_{KS} = T[n] + \int d^3 r V_{ext}(r) n(r) + E_H[n] + E_{xc}[n] + E_{II}, \tag{2.7}$$

where E_H[n] is called the Hartree energy and given by the following formula,

$$E_H[n] = \frac{e^2}{2} \int d^3 r d^3 r' \frac{n(r) n(r')}{\mid r - r' \mid}. \tag{2.8}$$

The Schrödinger like equation of non-interacting electrons is,

$$\hat{H}_{KS} \psi_i(r) = \varepsilon_i \psi_i(r), \tag{2.9}$$

where $\hat{H}_{KS}$ is effective Kohn-Sham Hamiltonian and ε_i is energy eigenvalues. The single-particle wave functions, or Kohn-Sham orbitals, are denoted by ψ_i(r). To make the equation simpler, spin operators are not taken into consideration. The relationship between Kohn-Sham orbitals and ground-state electron density is provided by,

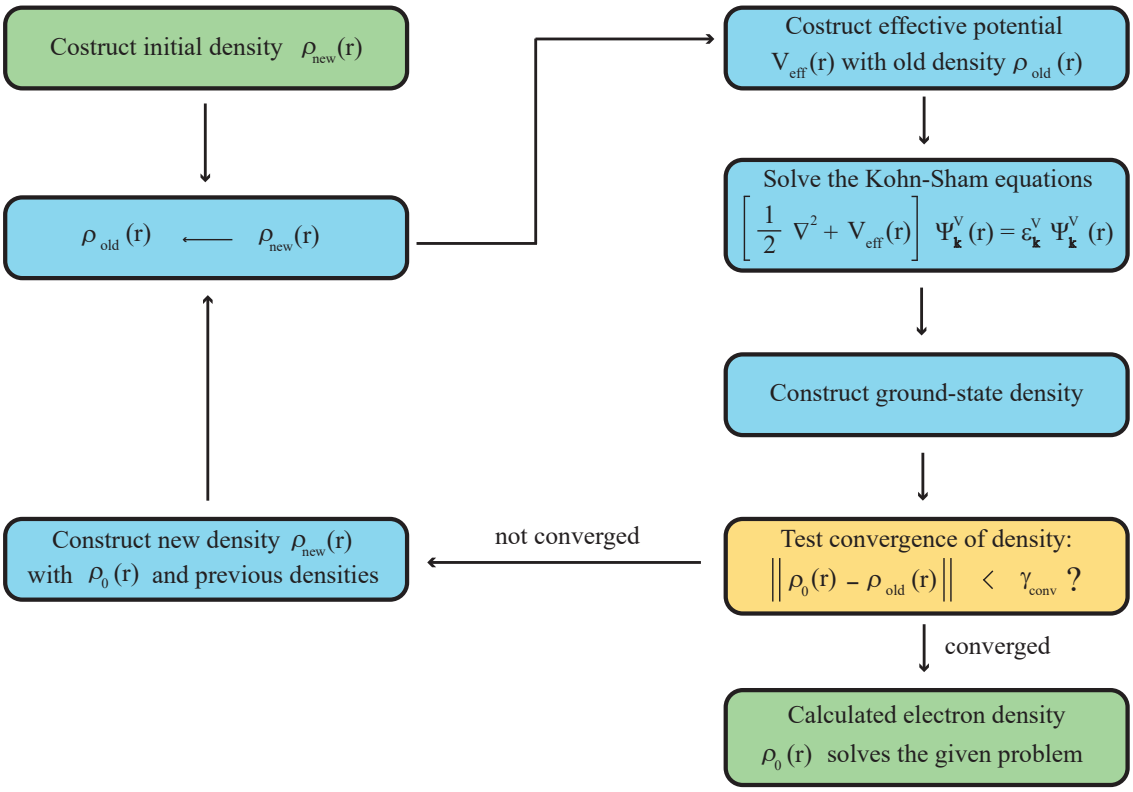

Figure 2.2. Schematic representation of the self-consistency cycle in Kohn-Sham DFT calculations. The arrow pointing back to the start of the cycle is a pictorial representation of the energy and force convergence criteria implemented in first principle calculations. The three dots in the fourth and sixth boxes indicate there are numerous terms that would not fit within the size of the box.

$$n(r) = \sum_{i=1}^{N} \mid \psi_i \mid^2, \tag{2.10}$$

and the effective Hamiltonian is,

$$\hat{H}_{KS}(r) = -\frac{1}{2}\nabla^2 + V_{KS}(r), \tag{2.11}$$

in which the effective Kohn-Sham effective potential, $V_{KS}(r)$,

$$V_{KS}(r) = V_{ext}(r) + V_H(r) + V_{xc}(r), \tag{2.12}$$

that is the total of the external, $V_{ext}(r)$ Hartree, $V_H(r)$ and exchange-correlation, $V_{xc}(r)$potentials, respectively.

An initial estimation of the electron density must be given. Then, for the specified electron density, V_{KS}(r) is generated to represent the effective Kohn-Sham potential. The results of each iteration are compared to those from the previous one to see if convergence has been achieved. This is followed by an iterative solution. The system's overall energy is then calculated using the resulting density.

A converging iterative solution path, which is shown schematically at Fig. 2.2, should be used to determine the exact ground-state density functional. The objective is to construct a Kohn-Sham Hamiltonian starting from a trial functional and identify the output electron density functional that provides the smallest amount of energy. The process should be repeated until the subsequent outputs converge in energy.

2.2.2.1. Exchange-Correlation Functionals

Kohn-Sham equations determine the final electron density of a system, which is then employed in the calculation of the total energy. In order to complete the Kohn-sham equation, exchange-correlation should be known. There are different approximations to calculate exchange-correlation energy. These functionals are widely used in DFT[49,76]. This section is devoted to two commonly used approximations used to determine the exchange-correlation functional of many-body systems.

Local Densiy Approximation (LDA): The one-electron Schrödinger equation and the LDA, which is the most frequently used, were both introduced in the same 1965 publication by Kohn and Sham[49]. According to LDA, electronic energy E_{xc} is uniformly dispersed in space, and as a result, E_{xc} is the functional of n(r) and can be produced from a homogeneous electron gas of the same density.

$$E_{xc}^{LDA}[n] = \int n(r)\varepsilon_{xc}^{hom}[n(r)]d^3r \tag{2.13}$$

where ε_{xc}^{hom} stands for the homogeneous exchange-correlation energy density of an electron density, n(r). While LDA may be used for a variety of bulk substances, it cannot be used to molecules because of the rapid variations in electron density. There are other limitations that need to be taken into consideration. For instance, LDA frequently leads to overbinding between atoms, and as a result, the estimated bond lengths are significantly less than the values obtained from experiments. LDA can also produce inconsistent outcomes for systems like strongly correlated systems or polarized dielectrics that include (consist of

more complex electronic interactions that are difficult to accurately characterize using LDA).

Generalized Gradient Approximation (GGA): Given that the spatial distribution of electron density is not uniform in real systems, GGA functional defines the E_{xc} to be the functional of both n(r) and the density gradient, $\nabla_{n(r)}$. The exchange-correlation energy is described by GGA as,

$$E_{xc}^{GGA}[n] = \int fGGA(n(r), \nabla n(r))d^3r \tag{2.14}$$

GGA satisfies the uniform electron gas standards as well.

2.2.3. Hellman-Feynman Theorem

The Hellmann-Feynman theorem is an essential component of DFT. It claims that the derivative of the total energy with respect to an external parameter is equal to the expectation value of the derivative of the Hamiltonian with respect to the same parameter. By taking into consideration the change in energy with respect to external perturbations, this theorem allows the calculation of forces and related properties. It provides a basis for methods such as molecular dynamics simulations and geometry optimization[34].

$$\frac{\partial E}{\partial \lambda} = \langle \frac{\partial \hat{H}}{\partial \lambda} \rangle \tag{2.15}$$

where $\frac{\partial E}{\partial \lambda}$ is the derivative of the total energy E with respect to an external parameter λ, $\langle \frac{\partial \hat{H}}{\partial \lambda} \rangle$ is the expectation value of the derivative of the Hamiltonian $\hat{H}$ with respect to the same parameter λ.

The Hellmann-Feynman theorem states that the derivative of the total energy with respect to an external parameter is equal to the expectation value of the derivative of the Hamiltonian with respect to the same parameter. By taking into consideration the change in energy with respect to external perturbations, this theorem offers a crucial relationship for computing characteristics such as forces or related variables.

2.2.4. Hybrid Functionals

It is possible to estimate the precise electronic band dispersions of solids through DFT calculations using LDA and GGA. However, each functional provides results on the width of the band gap that are underestimated due to poor accuracy and efficiency in determining the true exchange-correlation energy of the systems. Hybrid functionals have been used as an appropriate solution to address the disadvantages of traditional exchange-correlation functionals. Hybrid functionals come in a variety of numbers, including PBE0[1,22], B3LYP[6,56,7], and Heyd-Scuseria-Ernzerhof (HSE)[38,37,54] which perform well for a variety of systems because they produce results that are largely consistent and agree with examinations. The method of hybrid functionals is based on defining the exchange term of the system by combining a portion of the exact exchange from HF with the exchange calculated from the standard density functional (GGA or LDA), whereas the correlation part is entirely attained from the standard density functionals. For instance, HSE types create Perdew-Burke-Ernzerhof (PBE) functionals by combining 25% of the HF exact exchange with 75% of the GGA exchange. The most well-known HSE functionals are those which separate exchange interactions into short-range (SR) and long-range (LR) components, significantly reduce computation cost, and define the Coulomb operator as

$$\frac{1}{r} = SR_{\omega}(r) + LR_{\omega}(r) = \frac{1 - erf(\omega r)}{r} + \frac{erf(\omega r)}{r} \tag{2.16}$$

where $r = \mid r - r' \mid$, and ω is a controllable range-separation parameter (the optimum value is in between 0.2-0.3 $Å^{-1}$) that governs the extent of exchange interactions to mimic the effect of screening. The system's exchange-correlation energy is represented as follows:

$$E_{xc}^{HSE} = aE_{x}^{HF,SR}(\omega) + (1-a)E_{x}^{PBE,SR}(\omega) + E_{x}^{PBE,LR}(\omega) + E_{c}^{PBE} \tag{2.17}$$

In this equation, $E_{x}^{HF,SR}$ refers to the contribution from short-range HF exchange, $E_{x}^{PBE,SR}$ and $E_{x}^{PBE,LR}$ indicates that the short- and long-range parts of the PBE exchange energy, respectively, and E_c represents the PBE correlation energy.

2.3. Computing Phonons

The term "phonon" refers to the quantum mechanical description of lattice vibration. By analyzing a material's phonon band dispersion via the Brillouin Zone (BZ), one can deduce its vibrational properties. According to the theory, matter's atoms vibrate around an identified equilibrium point that is consistent with Hooke's law. Atomic displacements generate forces that return the system to equilibrium, comparable to a simple spring, and these oscillations follow Hooke's law;

$$F = -kx \tag{2.18}$$

where x is the distance between the atom and equilibrium position and k is the spring constant. This section discusses the DFT calculation method for phonon band dispersion.

Vibrations are not seen in the solution because DFT calculations are performed at absolute zero (0 K). However, as previously established, if an atom is moved from its equilibrium position, a restoring force follows that can be calculated. The small displacement method is the name of this technique. The displacement of just a few of atoms in a sufficiently large super cell provides the force constant matrix. The number of displaced atoms can vary depending on the system's symmetry. For each displacement, Hellmann-Feynman forces are estimated. Force matrix is constructed. Potential energy of a crystal in low temperatures is given by equation;

$$U_{harm} = E_{eq} + \frac{1}{2} \sum_{ls\alpha, l't\beta} \phi_{ls\alpha, l't\beta} \upsilon_{ls\alpha} \upsilon_{l't\beta} \tag{2.19}$$

where E_{eq} is the total energy of the crystal at equilibrium positions, υ_{ls} is the displacement of atom s in unit cell l, α, and β denotes the direction of the displacement in cartesian coordinates, $\phi_{ls\alpha, l't\beta}$ is the force constant matrix. Differentiation of the harmonic energy in Eq. 2.19 relation between the forces and the displacements can be deduced. The relation is linear, as $F_{ls\alpha}$ is found to be;

$$F_{ls\alpha} = -\sum_{l't\beta} \phi_{ls\alpha, l't\beta} \upsilon_{l't\beta} \tag{2.20}$$

Using the cohesive energy formula for the force constant matrix, dynamical matrix can be defined as;

$$D_{s\alpha,t\beta} = \frac{1}{\sqrt{M_s M_t}} \sum_{l} e^{iq(R_{l't\beta} - R_{ls\alpha})} \phi_{ls\alpha,l't\beta} \tag{2.21}$$

where M_s is the mass of s^{th}, M_t is the mass of t^{th} atom, $R_{l't\beta}$ - $R_{ls\alpha}$ is the distortion of the atoms. The phonon frequencies of each phonon branch can be estimated using eigenvalues after the dynamical matrix has been established. The totality of the degree of freedom of a crystal, which is 3*N* in a system constructed by the *N* atoms in the primitive cell, therefore defines the total number of phonon branches. Among these, 3 branches are acoustical, and 3*N* - 3 are optical. Atomic motions that are in-phase and out-of-phase are described by the acoustic and optical branches, respectively.

2.4. Computational Parameters

This section provides an overview of the methodology used in the thesis, structural optimization, and electronic band dispersion the first-principles calculations within the DFT as implemented in the Vienna Ab initio Simulation Package (VASP)[53,51]. The Plane-wave projector-augmented wave potentials were used and the exchange-correlation potential was approximated using the PBE form of the GGA[77].

In Chapter 3, the DFT-D2 method was used to implement the vdW corrections[32]. Charge transfers between Mo and S atoms forming Mo_8S_{12} layer and those with Li atom were investigated using Bader analysis[35]. The plane-wave functions were expanded up to a 500 eV of kinetic energy cutoff and the criterion for total energy convergence was taken to be 10^{-8} eV with the corresponding convergence of the forces to be less than 10^{-5} eV/Å. 20 Å of vacuum spacing was introduced to prevent interactions between repeating structures along the out-of-plane direction. During the ionic relaxations, the BZ was sampled using 7 $\times$ 7 $\times$ 1 k-points. The vibrational properties were calculated using the PHON code which is based on the small-displacement method[52,4]. In order to simulate Scanning Tunnelling Microscopy (STM) image, the primitive unit cell with partial charge densities in the range [-2,0] eV was considered.

CHAPTER 3

LITHIATED SINGLE-LAYER HOLEY MO_8S_{12}: ELECTRONIC, MAGNETIC AND VIBRATIONAL CHARACTERISTICS

Mechanical stability and atomic configuration of Li-intercalated electrode materials are also important attributes for evaluating the electrochemical performance of LIBs. The configuration and mechanical characteristics of TMDs upon lithiation were investigated using theoretical calculations and experimental methods[110,125,102]. Single-layer form of MoS_2 was considered as a solution to the scaling problem in electric field effect transistors (FETs), which has attracted great interest in the scientific community[80]. Zhao et al. showed that the phase stability of lithiated TMDs is strongly dependent on the number of layers, and the structural instability occurs with decreasing nanosheet thickness[125]. In addition, recently single- and multi-layers of MoS_2 have been used in lithium-ion battery applications due to the high lithium storage capacity[117,40,12,66,69]. Moreover, structural analysis revealed that structural phase transition occurs from 2H-phase to energetically less favorable 1T-phase in MoS_2 via the intercalation of Li atom[5,79,41,68,109,84].

Apart from widely studied 2D TMDs materials, such as MoS_2 and WS_2, novel holey phase of W-based chalcogenides, namely W_8Se_{12}, has been recently demonstrated[75]. Single-layer form of W_8Se_{12} was reported to be an integrated phase controllably created in a single-layer WSe_2. It was also reported that single-layers of W_8S_{12}, W_8Se_{12}, Mo_8S_{12}, and Mo_8Se_{12} were also predicted to possess direct band gap with outstanding anisotropic optical absorption in the visible spectrum. Furthermore, under uniaxial strain, direct-indirect-metal transitions were investigated for single-layer W_8Se_{12}[75]. Mendes et al. investigated the formation of rotational defects caused by chalcogen vacancies as a result of interaction of single-layer WSe_2 and electron beam[71]. It was claimed that the holey structure formed using single-layer WSe_2 can lead to significant changes in the properties of the material. Another study showed that it is important to create sub-nm holes at different temperatures for single-layer WS_2 and it was mentioned that future studies could explore methods of producing bulk holey structures by combining thermal processes with scalable fabrication methods such as electrochemical oxidation or ion bombardment[86]. In addition, Sapkota et al. prepared composite laminate membranes containing porous MoS_2 nanosheets and found

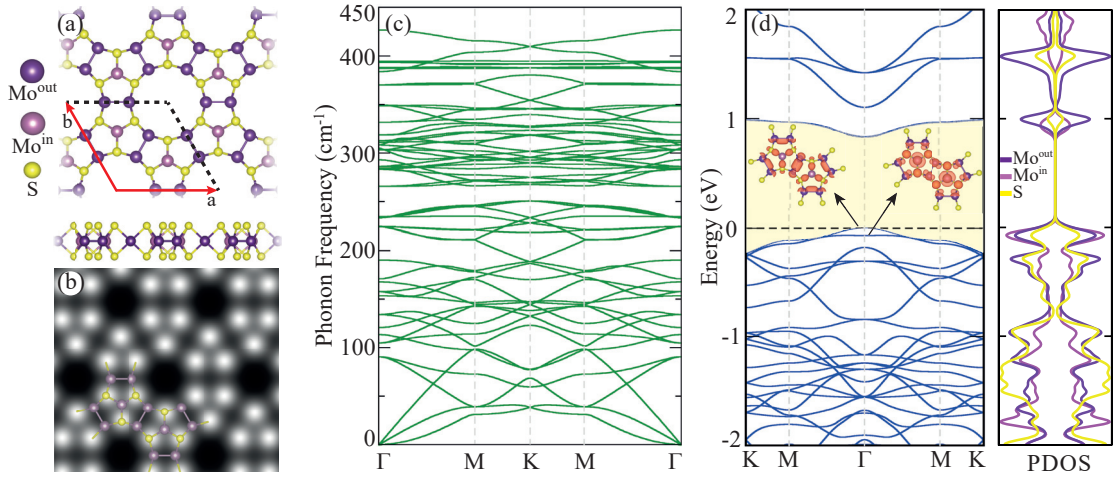

Figure 3.1. For the single-layer of Mo_8S_{12}: (a) Top and side views of the crystal structure. (b) The simulated STM image and (c) the phonon band structure. (d) The electronic band structure and corresponding partial density of states (PDOS). PDOS are normalized to unity in order to show the contribution of individual atoms.

high ion selectivity and ultra-high water permeability values that could be improved[87].

In this thesis, structural, electronic, and vibrational properties of two-dimensional bare and the lithiated structures of Mo_8S_{12} were investigated by *ab initio* calculations. Total energy optimizations and phonon band dispersion calculations revealed the structural and dynamical stability of free-standing Mo_8S_{12} layer. In addition, non-magnetic semiconducting Mo_8S_{12} was shown to turn into a ferromagnetic half-metal via one-sided lithiation and lithiation from both surfaces results in a semiconductor-to-metal transition.

3.1. Single-Layer Mo_8S_{12}

The crystal structure of the single-layer Mo_8S_{12} shown in Fig. 3.1(a) consists of a primitive unit cell containing 8 Mo and 12 S atoms. Two types of Mo atoms, 4-coordinated outer Mo atoms (Mo^{out}) and 6-coordinated inner Mo atoms (Mo^{in}), are denoted in two different colors (see Fig. 3.1(a)). The atomic configuration of single-layer Mo_8S_{12} has a sandwich-type formed by three atomic layers arranged as S-Mo-S. As listed in Table 3.1, the optimized in-plane lattice parameters, $a = b$, are calculated to be 9.22 Å which is much larger as compared to that of single-layer MoS_2 (3.19 Å)[120]. The corresponding Mo-S bond lengths are found to vary from 2.43 to 2.46 Å. Additionally, the distance between the outermost S atoms, namely the thickness of the single-layer Mo_8S_{12}, is found to be

Table 3.1. For the bare and lithiated single-layer of Mo_8S_{12}; optimized in-plane lattice parameters (a=b), thickness (t), the work function for the two surfaces (ϕ_{Li} and ϕ_S), calculated cohesive energy per atom (E_{Coh}), the amount of charge transfer from Li to Mo_8S_{12} ($\Delta\rho$), and electronic band gap calculated with GGA functionals (E_{Gap}), half-metallic (HM) behaviour of the one-side lithiated Mo_8S_{12} and metallic (M) behaviour of the double-side lithiated Mo_8S_{12}.

Mo_8S_{12}	a=b (Å)	t (Å)	μ (μ_b/cell)	ϕ_{Li} (eV)	ϕ_S (eV)	E_{Coh} (eV/atom)	E_{Gap} (eV)
Bare	9.22	3.25	0	-	5.93	4.77	0.83
One-sided	9.19	4.13	1	2.14	5.51	-	HM
Double-sided	9.23	4.92	0	2.72	-	-	M

3.25 Å. Bader charge analysis shows that the single-layer Mo_8S_{12} structure is formed such that each Mo atom donates an average of 0.9 e^- and each S atom gains 0.6 e^- charge, indicating the ionic bonding character between Mo and S atoms. Moreover, the cohesive energy is calculates using the formula, E_{Coh}=(mE_{Mo}+nE_S - $E_{Mo_8S_{12}}$)/($m+n$), where m and n stand for the number of Mo and S atoms, respectively contained in the primitive cell. In addition, E_{Mo} and E_S show the total energies of isolated Mo and S atoms, $E_{Mo_8S_{12}}$ is the ground state energy of single-layer Mo_8S_{12}. The cohesive energy per atom is calculated as 4.77 eV/atom. Compared to the cohesive energies of 1H (4.98 eV/atom)[3] and 1T (4.67 eV/atom) phases of MoS_2, single-layer Mo_8S_{12} has a closer cohesive energy, indicating its energetic feasibility. The work function of single-layer Mo_8S_{12} is calculated to be 5.93 eV which is higher than that of similar phases such as 1H-MoS_2 (5.12 eV)[48] and 1T-MoS_2 (5.04 eV)[115].

The dynamical stability of Mo_8S_{12} structure is determined via phonon band structure calculations. It is found that free-standing single-layer of Mo_8S_{12} is dynamically stable as all the phonon branches are free from imaginary frequencies through the whole BZ (see Fig. 3.1(c)). The single-layer Mo_8S_{12} possesses 57 optical phonon branches out of 3 acoustical phonons. The highest frequency optical phonon mode is found to have a frequency of 427 cm^{-1} at the Γ point an indication of Mo-S bond stretching.

Electronic properties of single-layer Mo_8S_{12} are investigated in terms of the electronic band dispersions and PDOS. As shown in Fig. 3.1(d), the valence band maximum (VBM) and conduction band minimum (CBM) reside at the Γ point of the BZ indicating the direct band gap nature of single-layer Mo_8S_{12} with a band gap of 0.83 eV. As compared to the predicted electronic band gap of single-layer MoS_2 (1.60 eV), Mo_8S_{12} possesses a

Table 3.2. For the adsorption of single Li atom on single-layer Mo_8S_{12}; adsorption positions of Li before and after the structural relaxations. The corresponding binding energies, E_b; and the amount of charge donated by Li atom to Mo_8S_{12} layer, ρ.

Initial Positions	Final Positions	E_b (eV)	ρ (e^-)
B_{Mo-Mo}	B_{Mo-Mo}	3.40	0.9
B_{Mo-S}	T_{Mo}	3.16	0.9
T_{Mo}	T_{Mo}	3.16	0.9
T_S	T_{Mo}	3.16	0.9
H_1	B_{Mo-Mo}	3.40	0.9
H_2	H_2	2.46	0.9

lower energy band gap. As shown by the PDOS, both VBM and CBM states are dominated by the Mo^{out} atoms, the S and Mo^{in} atoms have almost similar contributions in both the VBM and CBM states. Moreover, since the single-layer form of Mo_8S_{12} can be created within the structure of MoS_2 locally, the two phases form a lateral heterostructure whose band alignment type is found to be a type-II alignment. The VBM and CBM states of such lateral heterostructure arise from the MoS_2 and Mo_8S_{12}, respectively.

3.2. Interaction of Single-Layer Mo_8S_{12} with Single Lithium Atom

In order to understand the properties of one- and double-side lithiated single-layer Mo_8S_{12}, firstly the interaction of single Li atom with the Mo_8S_{12} surface is investigated using a supercell containing 32 Mo and 48 S atoms. For the investigation of the most stable adsorption site for single Li atom, six different sites are considered. The following adsorption sites, the bridge sites between Mo-Mo and Mo-S bonds (B_{Mo-Mo} and B_{Mo-S}, respectively), the top of a Mo atom (T_{Mo}), the top of a S atom (T_S) and two distinct hollow sites (H_1 and H_2), as shown in Fig. 3.2(a) are considered. Among the all adsorption sites, B_{Mo-Mo} is found to be the energetically most favorable site for the adsorption of a Li atom. Similarly, in single-layer MoS_2 top of a Mo atom was reported to be the ground state site for the adsorption of Li atom[73]. The binding energy of a single Li is calculated using the formula, $E_b = E_{Mo_8S_{12}} + E_{Li} - E_{system}$ where E_{system} represents the total energy of Li adsorbed single-layer Mo_8S_{12}. As listed in Table 3.2, initially adsorption of Li atom at the B_{Mo-S}, T_{Mo}, and T_S results in optimization at the T_{Mo} after full relaxation of the lattice and the ions. The corresponding binding energy of Li at the T_{Mo} site is 3.16 eV and that of

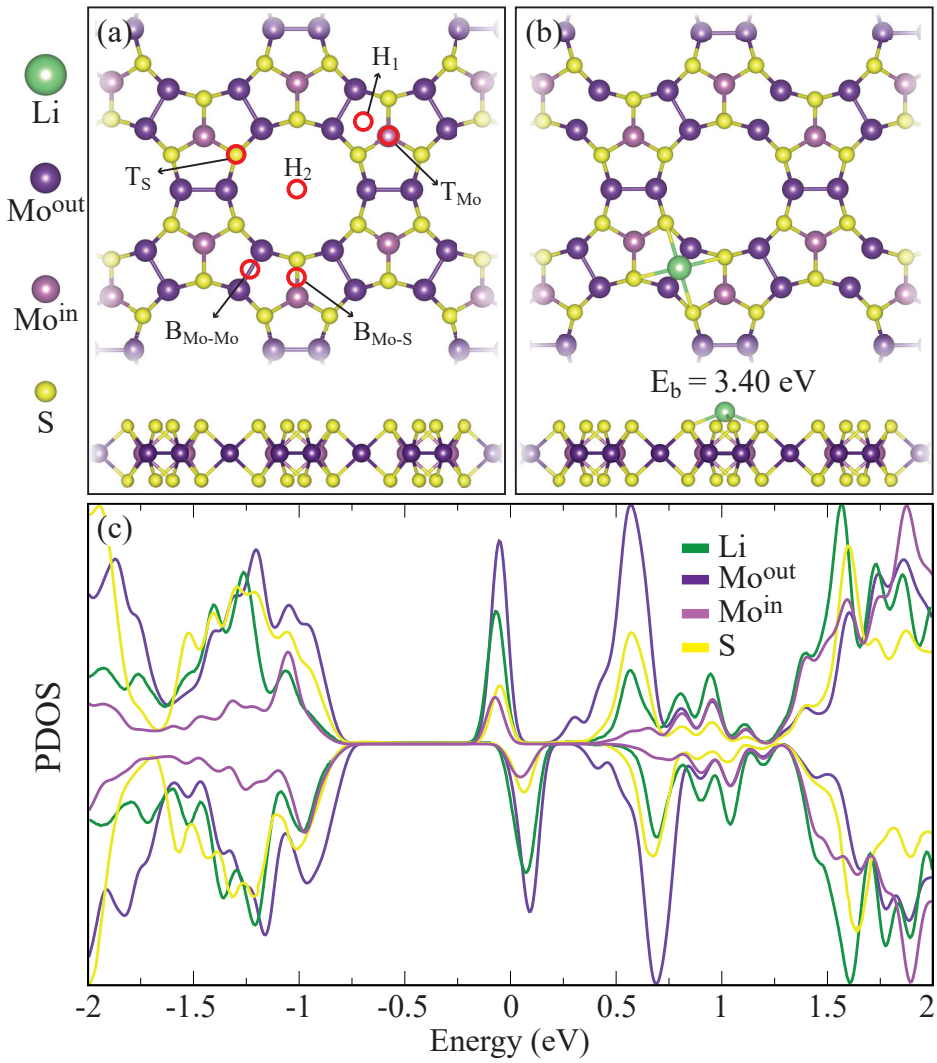

Figure 3.2. Top and side views of Li adsorption on Mo_8S_{12} for (a) various sites which are marked by red circles and (b) the energetically most stable structure. (c) The PDOS corresponding to Li adsorption in the Mo-Mo bridge side. PDOS are normalized to unity for the sake of clarity.

at the H_2 hollow site is 2.46 eV, lowest among all the considered sites. The Li atom when initially adsorbed at the remaining two adsorption sites, B_{Mo-Mo} and H_1 optimizes at the B_{Mo-Mo} site with the highest binding energy of 3.40 eV. The Bader charge analysis reveals that each Li atom donates 0.9 e^- to the Mo_8S_{12} structure indicating a strong bonding with the surface. Previously, the binding energy of a single Li atom on MoS_2 surface was reported to be 1.65 eV much lower than that on Mo_8S_{12} [73]. Electronically, it is found that the adsorbed single Li atom introduces mid-gap states to the electronic density of states of Mo_8S_{12} as shown in Fig. 3.2(c).

In order to determine the total energy profiles for the diffusion of a single Li through the surface of Mo_8S_{12}, three different migration pathways are considered including

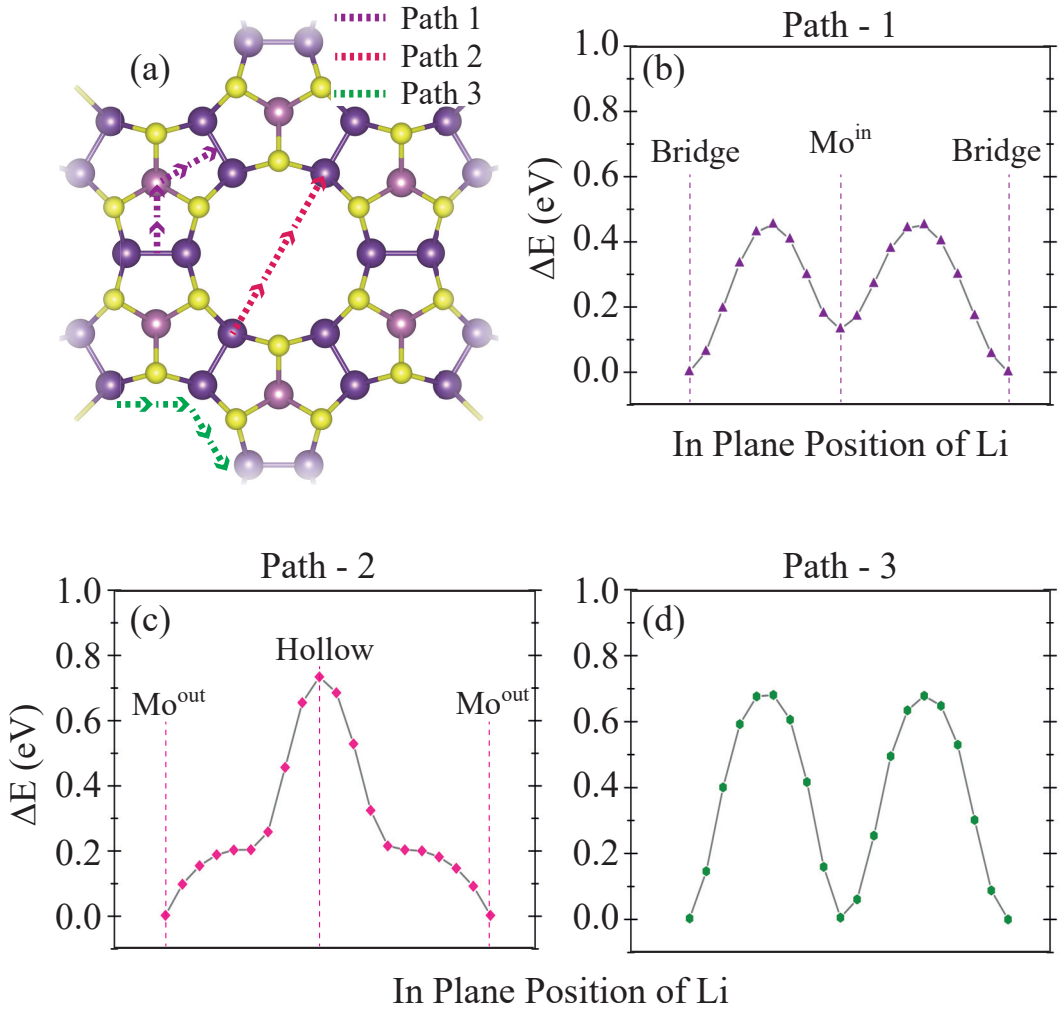

Figure 3.3. (a) Top view of single-layer Mo_8S_{12} describing three different diffusion paths for single Li atom. (b-d) Energy barrier profiles of Li adatom on single-layer Mo_8S_{12} through different paths.

different adsorption sites as shown in Fig. 3.3(a). Along the path 1 which is indicated by dashed purple lines, the migration of Li atom is considered between two Mo-Mo bridge sites through the top of Mo atom. As the Li atom diffuses along the path 1, there occurs an energy barrier of 0.45 eV as referenced with respect to the B_{Mo-Mo} site. In Path 2, the migration of Li atom starts from the top of a Mo atom and passes through the holey site and end at the top of a Mo atom. The barrier energy between the Mo-top sites is calculated to be 0.73 eV along the holey site as referenced with respect to the Mo-top site. It can be understood that the energy barrier along the holey site is much higher since Li is physisorbed at the H_2 site. Another migration path for the Li atom is chosen to be among the arc through Mo-S-Mo-S-Mo atomic arrangement on the holey part. As shown in panel Fig. 3.3(d), when Li atom migrates from top of a Mo to the another one, an energy barrier

of 0.68 eV is found as Li atom passes through the top-S site. The energy barrier for the migration of a single Li adsorbed on single-layer MoS_2 was reported to be 0.24 eV[73] much smaller than that of on Mo_8S_{12} layer.

3.3. One-Sided Lithiation

It is found from the single Li interaction that top of Mo-Mo bridge site is the energetically most favorable site for further lithiation of Mo_8S_{12} surface. A possible lithiation scenario could be to functionalize one surface of Mo_8S_{12} via Li atoms from each Mo-Mo bridge site. As shown in Fig. 3.4(a), on top of Mo-Mo bridge site, Li atom tends to bind with 4 neighbouring S atoms. Apparent from the charge density difference, one side Li adsorption on Mo_8S_{12} surface results in a magnetic structure whose magnetism is originated from the Mo-d orbitals. The lattice parameters are found to be slightly compressed, $a = b = 9.19$ Å, which is smaller than that of the bare structure. The thickness of the one-side lithiated Mo_8S_{12} (4.13 Å) is slightly larger than the bare structure indicating a vertical distance of 0.88 Å for Li atoms. As each Mo-Mo bridge site is saturated with a Li atom, the repeating Li atoms are separated by a distance of 4.6 Å forming triangular patterns on the surface. Bader charge analysis reveals that as a Li atom is chemisorbed on the Mo-Mo bridge site, there occurs a donation of 0.9 e^- from Li to the Mo_8S_{12} surface through S atoms. In addition, the calculated work functions are 2.14 and 5.51 eV from the Li and S surfaces, respectively, which indicates a strong build-in electric field in the structure. Moreover, the phonon band dispersions reveal the dynamical stability of one-side lithiated Mo_8S_{12}. The highest frequency optical phonon mode at the Γ point is calculated to be at 425 cm^{-1} which is very close to that of bare Mo_8S_{12} (427 cm^{-1}) which indicates that the Mo-S stretching is slightly suppressed by the Li adsorption.

Electronic band dispersions for the one-side lithiated Mo_8S_{12} are investigated in order to understand the effect of Li adsorption on the electronic features. As seen in Fig. 3.4(c), the ferromagnetic state of one-side lithiated Mo_8S_{12} gives rise to the separation of majority and minority spin states and results in half-metallic behavior of the structure. Apparently, the majority spin states (solid blue lines) display metallic behavior while the minority spin states (dashed red lines) exhibit semiconducting nature with an electronic band gap of 0.57 eV. In addition, the calculated PDOS show that adsorbed Li atoms mostly contribute to the deep energy states of both valence and conduction levels and less contribution of Li atoms is found in the mid-gap states below the Fermi level. It is

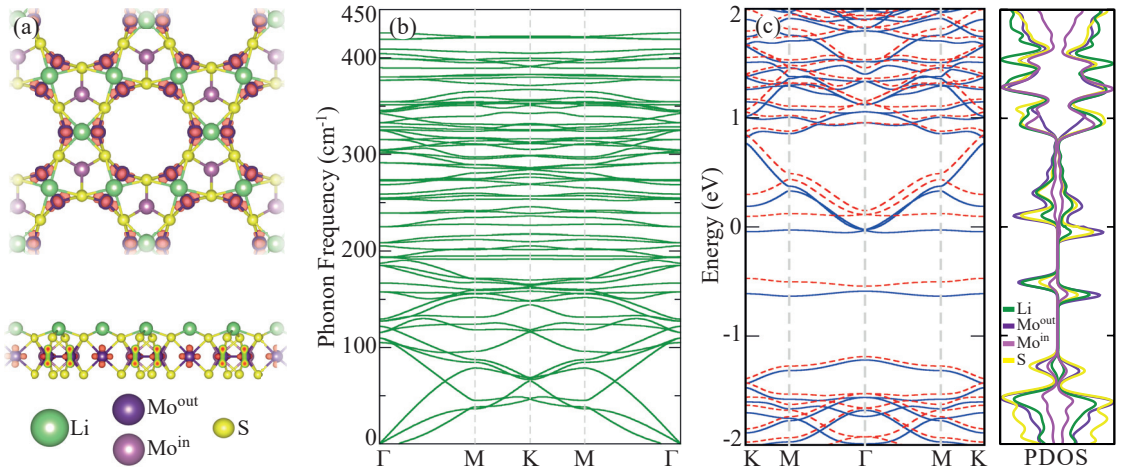

Figure 3.4. For the one-side lithiated single-layer of Mo_8S_{12}; (a) Top and side views of magnetization charge density at the isosurface value of 5×10^{-3}e Å^{-3}. (b) The phonon band structure. (c) The electronic band structure and the normalized PDOS. Solid blue and dashed red lines stand for opposite spin states, respectively.

seen that one-sided lithiation can turn non-magnetic semiconducting Mo_8S_{12} layer into a ferromagnetic half-metal.

3.4. Double-Sided Lithiation

As the both surfaces of single-layer Mo_8S_{12} are functionalized with Li atoms through Mo-Mo bridge sites, a dynamically stable out-of-plane symmetric structure is obtained (see Fig. 3.5(a)). Phonon band structures show the dynamical stability of the single-layer double-side lithiated Mo_8S_{12}. The highest frequency phonon mode of double-side lithiated Mo_8S_{12} is found to significantly red shift (404 cm^{-1}) as a result of suppressed Mo-S stretching and expanding lattice. The in-plane lattice parameters slightly increase to 9.23 Å indicating that a very small surface strain occurs via full lithiation. As the full lithiation is formed, each Li atom is found to donate 0.3 e$^-$ to the surface of Mo_8S_{12}. Since both sides are lithiated, the work function of each surfaces are calculated to be equal to each other (2.72 eV), which is quite larger than that of one-side lithiated Mo_8S_{12} (2.14 eV). In addition, magnetic ground state calculations show that both-sided lithiation of Mo_8S_{12} gives rise to the charge balance and non-magnetic state becomes energetically favorable.

Electronically, the double-side lithiated Mo_8S_{12} is found to be a metal whose conduction band minimum crosses the Fermi energy at the Γ point of the BZ (see Fig.

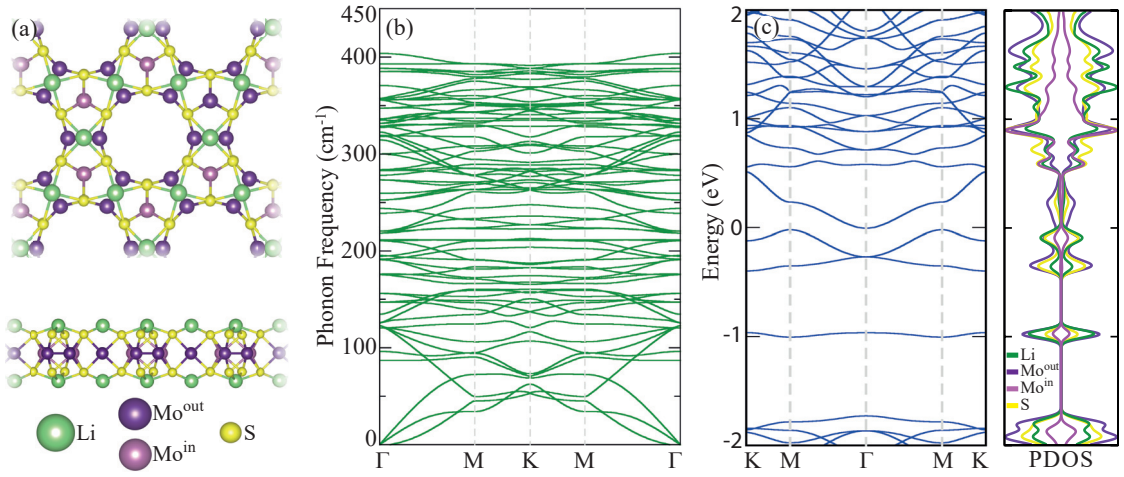

Figure 3.5. For the double-side lithiated single-layer of Mo_8S_{12}; (a) Top and side views of the crystal structure. (b) The phonon band structure and (c) the electronic band structure with normalized PDOS of the individual atoms.

3.5(c)). Similar to the case of one-side lithiated structure, the adsorbed Li atoms are found to contribute to the deep occupied energy states while tiny contributions are shown to occur in the highest two valence states.

3.5. Conclusion

In conclusion, the structural, vibrational, and electronic properties of free-standing single-layer Mo_8S_{12} were investigated, and it was shown that Mo_8S_{12} possesses a dynamically stable holey structure in free-standing form. The electronic band dispersions revealed the direct band gap semiconducting nature of the structure. In order to investigate the lithiation capacity of Mo_8S_{12}, firstly the interaction of the surface with a single Li atom was obtained by taking into account various adsorption sites. Total energy optimizations indicated that Li atom tends to be chemisorbed on 5-coordinated Mo-Mo bridge site and found to be thermally stable at the adsorption site. Next, the one-side lithiated structure of Mo_8S_{12} was constructed and the optimized single-layer was shown to be a stable ferromagnetic half-metal. The double-sided lithation was investigated by saturating all Mo-Mo bridge sites with Li atoms from two surfaces and the resultant structure was found to be a stable metal with non-magnetic interaction. Apparently, functionalization of one surface of Mo_8S_{12} gives rise to significant changes in the electronic and magnetic features.

CHAPTER 4

OVERALL DISCUSSION

Overall, motivated by the outstanding physics of electrons in low-dimensions, this master thesis focused on the investigation and the characterization of different types of novel ultra-thin crystals by means of DFT-based first-principles calculations.

In Chapter 1, a short introduction is written related to the 2D materials while Chapter 2 is the methodology of the DFT. In the work given in Chapter 3, investigations into the structural, vibrational, and electrical characteristics of free-standing single-layer Mo_8S_{12} revealed that it has a dynamically stable holey structure. Moreover, the Mo_8S_{12} structure is a direct band gap semiconductor, as shown by the electronic band dispersions. In order to examine the Mo_8S_{12}'s ability to be lithiated, it is necessary to determine how the surface interact with a single Li atom while accounting for numerous adsorption sites. The Li atom is found to be thermally stable at the adsorption location, and total energy optimizations suggested that it tended to be chemisorbed on a 5-coordinated Mo-Mo bridge site. The Mo_8S_{12} one-side lithiated structure is then built, and the optimized single-layer is demonstrated to be a stable ferromagnetic half-metal. By saturating all Mo-Mo bridge sites with Li atoms from two surfaces, the two-sided lithation is examined, and the resulting structure was discovered to be a stable metal with non-magnetic interaction.

To conclude, this thesis study proposes novel graphene-like single-layer and holey structures based on the first-principles calculations. Considering the general properties of holey Mo_8S_{12}, it becomes clear that it can be used in LIBs, supercapacitors, sensors and membrane applications, and it serves as an inspiration for other holey materials in this application field.

REFERENCES

(1) Adamo, C. and V. Barone (1999). Toward reliable density functional methods without adjustable parameters: The pbe0 model. *The Journal of chemical physics 110*(13), 6158–6170.

(2) Adilla, S. J., E. Nurfani, R. Kurniawan, C. D. Satrya, and Y. Darma (2017). Structural and optical properties analysis of mos2 nanoflakes on quartz substrate as prepared by mechanical exfoliation. In *Journal of Physics: Conference Series*, Volume 877, pp. 012036. IOP Publishing.

(3) Ahmad, S. and S. Mukherjee (2014). A comparative study of electronic properties of bulk mos2 and its monolayer using dft technique: application of mechanical strain on mos2 monolayer.

(4) Alfè, D. (2009). Phon: A program to calculate phonons using the small displacement method. *Computer Physics Communications 180*(12), 2622–2633.

(5) Ataca, C., H. Sahin, and S. Ciraci (2012). Stable, single-layer mx2 transition-metal oxides and dichalcogenides in a honeycomb-like structure. *The Journal of Physical Chemistry C 116*(16), 8983–8999.

(6) Becke, A. D. (1988). Density-functional exchange-energy approximation with correct asymptotic behavior. *Physical review A 38*(6), 3098.

(7) Beeke, A. D. (1993). Density-functional thermochemistry. iii. the role of exact exchange. *J. Chem. Phys 98*(7), 5648–6.

(8) Bernardi, M., M. Palummo, and J. C. Grossman (2013). Extraordinary sunlight absorption and one nanometer thick photovoltaics using two-dimensional monolayer materials. *Nano letters 13*(8), 3664–3670.

(9) Bolotsky, A., D. Butler, C. Dong, K. Gerace, N. R. Glavin, C. Muratore, J. A. Robinson, and A. Ebrahimi (2019). Two-dimensional materials in biosensing and healthcare: from in vitro diagnostics to optogenetics and beyond. *Acs Nano 13*(9), 9781–9810.

(10) Cao, X., C. Tan, X. Zhang, W. Zhao, and H. Zhang (2016). Solution-processed two-dimensional metal dichalcogenide-based nanomaterials for energy storage and conversion. *Advanced Materials 28*(29), 6167–6196.

(11) Chang, C.-Y., H.-T. Lin, M.-S. Lai, C.-L. Yu, C.-R. Wu, H.-C. Chou, S.-Y. Lin, C. Chen, and M.-H. Shih (2019). Large-area and strain-reduced two-dimensional molybdenum disulfide monolayer emitters on a three-dimensional substrate. *ACS applied materials & interfaces 11*(29), 26243–26249.

(12) Chang, K. and W. Chen (2011). L-cysteine-assisted synthesis of layered mos2/graphene composites with excellent electrochemical performances for lithium ion batteries. *ACS nano 5*(6), 4720–4728.

(13) Charlier, J.-C. (2002). Defects in carbon nanotubes. *Accounts of chemical research 35*(12), 1063–1069.

(14) Chen, F., Y. Yao, W. Su, S. Zhao, S. Ding, and L. Fu (2020). The synthesis of 2d mos2 flakes with tunable layer numbers via pulsed-argon-flow assisted cvd approach. *Ceramics International 46*(10), 14523–14528.

(15) Cheng, L., G. Liu, J. Zhao, and W. Jin (2021). Two-dimensional-material membranes: manipulating the transport pathway for molecular separation. *Accounts of Materials Research 2*(2), 114–128.

(16) Chhowalla, M., Z. Liu, and H. Zhang (2015). Two-dimensional transition metal dichalcogenide (tmd) nanosheets. *Chemical Society Reviews 44*(9), 2584–2586.

(17) Chhowalla, M., H. S. Shin, G. Eda, L.-J. Li, K. P. Loh, and H. Zhang (2013). The chemistry of two-dimensional layered transition metal dichalcogenide nanosheets. *Nature chemistry 5*(4), 263–275.

(18) Cohen-Tanugi, D. and J. C. Grossman (2012). Water desalination across nanoporous graphene. *Nano letters 12*(7), 3602–3608.

(19) Conley, H. J., B. Wang, J. I. Ziegler, R. F. Haglund Jr, S. T. Pantelides, and K. I. Bolotin (2013). Bandgap engineering of strained monolayer and bilayer mos2. *Nano letters 13*(8), 3626–3630.

(20) Coutinho, S., M. Tavares, C. Barboza, N. Frazão, E. Moreira, and D. L. Azevedo (2017). 3r and 2h polytypes of mos2: Dft and dfpt calculations of structural, optoelectronic, vibrational and thermodynamic properties. *Journal of Physics and Chemistry of Solids 111*, 25–33.

(21) Enyashin, A. N., L. Yadgarov, L. Houben, I. Popov, M. Weidenbach, R. Tenne, M. Bar-Sadan, and G. Seifert (2011). New route for stabilization of 1t-ws2 and mos2 phases. *The Journal of Physical Chemistry C 115*(50), 24586–24591.

(22) Ernzerhof, M. and G. E. Scuseria (1999). Assessment of the perdew–burke–ernzerhof exchange-correlation functional. *The Journal of chemical physics 110*(11), 5029–5036.

(23) Fermi, E. (1927). Statistical method to determine some properties of atoms. *Rend. Accad. Naz. Lincei 6*(602-607), 5.

(24) Ferrari, A. C., F. Bonaccorso, V. Fal'Ko, K. S. Novoselov, S. Roche, P. Bøggild, S. Borini, F. H. Koppens, V. Palermo, N. Pugno, et al. (2015). Science and technology roadmap for graphene, related two-dimensional crystals, and hybrid systems. *Nanoscale 7*(11), 4598–4810.

(25) Fivaz, R. and E. Mooser (1967). Mobility of charge carriers in semiconducting layer structures. *Physical Review 163*(3), 743.

(26) Forouzandeh, P. and S. C. Pillai (2021). Two-dimensional (2d) electrode materials for supercapacitors. *Materials Today: Proceedings 41*, 498–505.

(27) Galashev, A. and A. Vorob'ev (2021). First principle modeling of a silicene anode for lithium ion batteries. *Electrochimica Acta 378*, 138143.

(28) Ganatra, R. and Q. Zhang (2014). Few-layer mos2: a promising layered semiconductor. *ACS nano 8*(5), 4074–4099.

(29) Gao, J., Y. Zhou, Z. Li, S. Yan, N. Wang, and Z. Zou (2012). High-yield synthesis of millimetre-long, semiconducting carbon nitride nanotubes with intense photoluminescence emission and reproducible photoconductivity. *Nanoscale 4*(12), 3687–3692.

(30) Gaur, A. P., S. Sahoo, M. Ahmadi, S. P. Dash, M. J.-F. Guinel, and R. S. Katiyar (2014). Surface energy engineering for tunable wettability through controlled synthesis of mos2. *Nano letters 14*(8), 4314–4321.

(31) Geim, A. K. and I. V. Grigorieva (2013). Van der waals heterostructures. *Nature 499*(7459), 419–425.

(32) Grimme, S., J. Antony, S. Ehrlich, and H. Krieg (2010). A consistent and accurate ab initio parametrization of density functional dispersion correction (dft-d) for the 94 elements h-pu. *The Journal of chemical physics 132*(15), 154104.

(33) Han, J. K., S. Kim, S. Jang, Y. R. Lim, S.-W. Kim, H. Chang, W. Song, S. S. Lee, J. Lim, K.-S. An, et al. (2019). Tunable piezoelectric nanogenerators using flexoelectricity of well-ordered hollow 2d mos2 shells arrays for energy harvesting. *Nano Energy 61*, 471–477.

(34) Hellman, H. and R. Feynman (1939). The operator method in quantum mechanics. *Physical Review 56*(7), 340–344.

(35) Henkelman, G., A. Arnaldsson, and H. Jónsson (2006). A fast and robust algorithm for bader decomposition of charge density. *Computational Materials Science 36*(3), 354–360.

(36) Hernandez, Y., V. Nicolosi, M. Lotya, F. M. Blighe, Z. Sun, S. De, I. T. McGovern, B. Holland, M. Byrne, Y. K. Gun'Ko, et al. (2008). High-yield production of graphene by liquid-phase exfoliation of graphite. *Nature nanotechnology 3*(9), 563–568.

(37) Heyd, J. and G. E. Scuseria (2004). Efficient hybrid density functional calculations in solids: Assessment of the heyd–scuseria–ernzerhof screened coulomb hybrid functional. *The Journal of chemical physics 121*(3), 1187–1192.

(38) Heyd, J., G. E. Scuseria, and M. Ernzerhof (2003). Hybrid functionals based on a screened coulomb potential. *The Journal of chemical physics 118*(18), 8207–8215.

(39) Hohenberg, P. and W. Kohn (1964). Inhomogeneous electron gas. *Physical review 136*(3B), B864.

(40) Hwang, H., H. Kim, and J. Cho (2011). Mos2 nanoplates consisting of disordered graphene-like layers for high rate lithium battery anode materials. *Nano letters 11*(11), 4826–4830.

(41) Imanishi, N., M. Toyoda, Y. Takeda, and O. Yamamoto (1992). Study on lithium intercalation into mos2. *Solid State Ionics 58*(3-4), 333–338.

(42) Jaramillo, T. F., K. P. Jørgensen, J. Bonde, J. H. Nielsen, S. Horch, and I. Chorkendorff (2007). Identification of active edge sites for electrochemical h2 evolution from mos2 nanocatalysts. *science 317*(5834), 100–102.

(43) Jawaid, A., D. Nepal, K. Park, M. Jespersen, A. Qualley, P. Mirau, L. F. Drummy, and R. A. Vaia (2016). Mechanism for liquid phase exfoliation of mos2. *Chemistry of Materials 28*(1), 337–348.

(44) Jellinek, F., G. Brauer, and H. Müller (1960). Molybdenum and niobium sulphides. *Nature 185*(4710), 376–377.

(45) Johari, P. and V. B. Shenoy (2012). Tuning the electronic properties of semiconducting transition metal dichalcogenides by applying mechanical strains. *ACS nano 6*(6), 5449–5456.

(46) Jung, Y., J. Shen, Y. Liu, J. M. Woods, Y. Sun, and J. J. Cha (2014). Metal seed layer thickness-induced transition from vertical to horizontal growth of mos2 and ws2. *Nano letters 14*(12), 6842–6849.

(47) Kang, K., S. Xie, L. Huang, Y. Han, P. Y. Huang, K. F. Mak, C.-J. Kim, D. Muller, and J. Park (2015). High-mobility three-atom-thick semiconducting films with wafer-scale homogeneity. *Nature 520*(7549), 656–660.

(48) Kim, H.-g. and H. J. Choi (2021). Thickness dependence of work function, ionization energy, and electron affinity of mo and w dichalcogenides from dft and gw calculations. *Physical Review B 103*(8), 085404.

(49) Kohn, W. and L. J. Sham (1965). Self-consistent equations including exchange and correlation effects. *Physical review 140*(4A), A1133.

(50) Kong, D., H. Wang, J. J. Cha, M. Pasta, K. J. Koski, J. Yao, and Y. Cui (2013). Synthesis of mos2 and mose2 films with vertically aligned layers. *Nano letters 13*(3), 1341–1347.

(51) Kresse, G. and J. Furthmüller (1996). Efficient iterative schemes for ab initio total-energy calculations using a plane-wave basis set. *Physical review B 54*(16), 11169.

(52) Kresse, G., J. Furthmüller, and J. Hafner (1995). Ab initio force constant approach to phonon dispersion relations of diamond and graphite. *Europhysics Letters 32*(9), 729.

(53) Kresse, G. and J. Hafner (1993). Ab initio molecular dynamics for liquid metals. *Physical review B 47*(1), 558.

(54) Krukau, A. V., O. A. Vydrov, A. F. Izmaylov, and G. E. Scuseria (2006). Influence of the exchange screening parameter on the performance of screened hybrid functionals. *The Journal of chemical physics 125*(22), 224106.

(55) Lee, C., H. Yan, L. E. Brus, T. F. Heinz, J. Hone, and S. Ryu (2010). Anomalous lattice vibrations of single-and few-layer mos2. *ACS nano 4*(5), 2695–2700.

(56) Lee, C., W. Yang, and R. G. Parr (1988). Development of the colle-salvetti correlation-energy formula into a functional of the electron density. *Physical review B 37*(2), 785.

(57) Lee, Y.-H., X.-Q. Zhang, W. Zhang, M.-T. Chang, C.-T. Lin, K.-D. Chang, Y.-C. Yu, J. T.-W. Wang, C.-S. Chang, L.-J. Li, et al. (2012). Synthesis of large-area mos2 atomic layers with chemical vapor deposition. *Advanced materials 24*(17), 2320–2325.

(58) Li, H., H. Wu, S. Yuan, and H. Qian (2016). Synthesis and characterization of vertically standing mos2 nanosheets. *Scientific reports 6*(1), 21171.

(59) Li, J., C. Cao, and H. Zhu (2007). Synthesis and characterization of graphite-like carbon nitride nanobelts and nanotubes. *Nanotechnology 18*(11), 115605.

(60) Li, T. (2012). Ideal strength and phonon instability in single-layer mos 2. *Physical*

Review B 85(23), 235407.

(61) Li, T. and G. Galli (2007). Electronic properties of mos2 nanoparticles. *The Journal of Physical Chemistry C 111*(44), 16192–16196.

(62) Li, W., G. Zhang, M. Guo, and Y.-W. Zhang (2014). Strain-tunable electronic and transport properties of mos 2 nanotubes. *Nano Research 7*, 518–527.

(63) Li, X., W. Cai, J. An, S. Kim, J. Nah, D. Yang, R. Piner, A. Velamakanni, I. Jung, E. Tutuc, et al. (2009). Large-area synthesis of high-quality and uniform graphene films on copper foils. *science 324*(5932), 1312–1314.

(64) Lin, Y.-C., W. Zhang, J.-K. Huang, K.-K. Liu, Y.-H. Lee, C.-T. Liang, C.-W. Chu, and L.-J. Li (2012). Wafer-scale mos 2 thin layers prepared by moo 3 sulfurization. *Nanoscale 4*(20), 6637–6641.

(65) Liu, K.-K., W. Zhang, Y.-H. Lee, Y.-C. Lin, M.-T. Chang, C.-Y. Su, C.-S. Chang, H. Li, Y. Shi, H. Zhang, et al. (2012). Growth of large-area and highly crystalline mos2 thin layers on insulating substrates. *Nano letters 12*(3), 1538–1544.

(66) Lopez-Sanchez, O., D. Lembke, M. Kayci, A. Radenovic, and A. Kis (2013). Ultrasensitive photodetectors based on monolayer mos2. *Nature nanotechnology 8*(7), 497–501.

(67) Lu, P., X. Wu, W. Guo, and X. C. Zeng (2012). Strain-dependent electronic and magnetic properties of mos 2 monolayer, bilayer, nanoribbons and nanotubes. *Physical Chemistry Chemical Physics 14*(37), 13035–13040.

(68) Lukowski, M. A., A. S. Daniel, F. Meng, A. Forticaux, L. Li, and S. Jin (2013). Enhanced hydrogen evolution catalysis from chemically exfoliated metallic mos2 nanosheets. *Journal of the American Chemical Society 135*(28), 10274–10277.

(69) Mak, K. F., K. He, J. Shan, and T. F. Heinz (2012). Control of valley polarization in monolayer mos2 by optical helicity. *Nature nanotechnology 7*(8), 494–498.

(70) Mak, K. F., C. Lee, J. Hone, J. Shan, and T. F. Heinz (2010). Atomically thin mos 2: a new direct-gap semiconductor. *Physical review letters 105*(13), 136805.

(71) Mendes, R. G., J. Pang, A. Bachmatiuk, H. Q. Ta, L. Zhao, T. Gemming, L. Fu, Z. Liu, and M. H. Rummeli (2019). Electron-driven in situ transmission electron microscopy of 2d transition metal dichalcogenides and their 2d heterostructures. *ACS nano 13*(2), 978–995.

(72) Najmaei, S., Z. Liu, W. Zhou, X. Zou, G. Shi, S. Lei, B. I. Yakobson, J.-C. Idrobo, P. M. Ajayan, and J. Lou (2013). Vapour phase growth and grain boundary structure of molybdenum disulphide atomic layers. *Nature materials 12*(8), 754–759.

(73) Nasr Esfahani, D., O. Leenaerts, H. Sahin, B. Partoens, and F. Peeters (2015). Structural transitions in monolayer mos2 by lithium adsorption. *The Journal of Physical Chemistry C 119*(19), 10602–10609.

(74) Pan, H. and Y.-W. Zhang (2012). Tuning the electronic and magnetic properties of mos2 nanoribbons by strain engineering. *The Journal of Physical Chemistry C 116*(21), 11752–11757.

(75) Peng, Y., Q. Zhu, W. Xu, and J. Cao (2022). High anisotropic optoelectronics in monolayer binary m8x12 (m= mo, w; x= s, se, te). *ACS Applied Materials & Interfaces 14*(23), 27056–27062.

(76) Perdew, J., K. Burke, and M. Ernzerhof (1996a). Generalized gradient approximation made simple. *Physical Review Letters 77*(18), 3865–3868.

(77) Perdew, J. P., K. Burke, and M. Ernzerhof (1996b). Generalized gradient approximation made simple. *Physical review letters 77*(18), 3865.

(78) Pospischil, A., M. M. Furchi, and T. Mueller (2014). Solar-energy conversion and light emission in an atomic monolayer p–n diode. *Nature nanotechnology 9*(4), 257–261.

(79) Py, M. and R. Haering (1983). Structural destabilization induced by lithium intercalation in mos2 and related compounds. *Canadian Journal of Physics 61*(1), 76–84.

(80) Radisavljevic, B. and A. Kis (2013). Mobility engineering and a metal–insulator transition in monolayer mos2. *Nature materials 12*(9), 815–820.

(81) Ramakrishna Matte, H., A. Gomathi, A. K. Manna, D. J. Late, R. Datta, S. K. Pati, and C. Rao (2010). Mos2 and ws2 analogues of graphene. *Angewandte Chemie International Edition 49*(24), 4059–4062.

(82) Ran, J., T. Y. Ma, G. Gao, X.-W. Du, and S. Z. Qiao (2015). Porous p-doped graphitic carbon nitride nanosheets for synergistically enhanced visible-light photocatalytic h 2 production. *Energy & Environmental Science 8*(12), 3708–3717.

(83) Ren, W. and H.-M. Cheng (2014). The global growth of graphene. *Nature nanotechnology 9*(10), 726–730.

(84) Rocquefelte, X., F. Boucher, P. Gressier, G. Ouvrard, P. Blaha, and K. Schwarz (2000). Mo cluster formation in the intercalation compound limos 2. *Physical Review B 62*(4), 2397.

(85) Rojaee, R. and R. Shahbazian-Yassar (2020). Two-dimensional materials to address the lithium battery challenges. *ACS nano 14*(3), 2628–2658.

(86) Ryu, G. H., A. France-Lanord, Y. Wen, S. Zhou, J. C. Grossman, and J. H. Warner (2018). Atomic structure and dynamics of self-limiting sub-nanometer pores in monolayer ws2. *ACS nano 12*(11), 11638–11647.

(87) Sapkota, B., W. Liang, A. VahidMohammadi, R. Karnik, A. Noy, and M. Wanunu (2020). High permeability sub-nanometre sieve composite mos2 membranes. *Nature communications 11*(1), 2747.

(88) Scalise, E., M. Houssa, G. Pourtois, V. Afanas' ev, and A. Stesmans (2012). Strain-induced semiconductor to metal transition in the two-dimensional honeycomb structure of mos 2. *Nano Research 5*, 43–48.

(89) Schmidt-Mende, L. and J. L. MacManus-Driscoll (2007). Zno–nanostructures, defects, and devices. *Materials today 10*(5), 40–48.

(90) Scott, A. (2016). Graphene's global race to market. *Chem. Eng. News 94*(15), 28–33.

(91) Shanmugam, V., R. A. Mensah, K. Babu, S. Gawusu, A. Chanda, Y. Tu, R. E. Neisiany, M. Försth, G. Sas, and O. Das (2022). A review of the synthesis, properties, and

applications of 2d materials. *Particle & Particle Systems Characterization 39*(6), 2200031.

(92) Shen, J., J. Wu, M. Wang, P. Dong, J. Xu, X. Li, X. Zhang, J. Yuan, X. Wang, M. Ye, et al. (2016). Surface tension components based selection of cosolvents for efficient liquid phase exfoliation of 2d materials. *Small 12*(20), 2741–2749.

(93) Shi, H., H. Pan, Y.-W. Zhang, and B. I. Yakobson (2013). Quasiparticle band structures and optical properties of strained monolayer mos 2 and ws 2. *Physical Review B 87*(15), 155304.

(94) Smith, R. J., P. J. King, M. Lotya, C. Wirtz, U. Khan, S. De, A. O'Neill, G. S. Duesberg, J. C. Grunlan, G. Moriarty, et al. (2011). Large-scale exfoliation of inorganic layered compounds in aqueous surfactant solutions. *Advanced materials 23*(34), 3944–3948.

(95) Song, I., C. Park, and H. Choi (2015). Synthesis and properties of molybdenum disulphide: from bulk to atomic layers. rsc adv 5: 7495–7514.

(96) Splendiani, A., L. Sun, Y. Zhang, T. Li, J. Kim, C.-Y. Chim, G. Galli, and F. Wang (2010). Emerging photoluminescence in monolayer mos2. *Nano letters 10*(4), 1271–1275.

(97) Stankovich, S., D. A. Dikin, G. H. Dommett, K. M. Kohlhaas, E. J. Zimney, E. A. Stach, R. D. Piner, S. T. Nguyen, and R. S. Ruoff (2006). Graphene-based composite materials. *nature 442*(7100), 282–286.

(98) Surwade, S. P., S. N. Smirnov, I. V. Vlassiouk, R. R. Unocic, G. M. Veith, S. Dai, and S. M. Mahurin (2015). Water desalination using nanoporous single-layer graphene. *Nature nanotechnology 10*(5), 459–464.

(99) Tang, H. and S. R. Morrison (1993). Optimization of the anisotropy of composite mos2 films. *Thin Solid Films 227*(1), 90–94.

(100) Tao, Y., Z.-Y. Sui, and B.-H. Han (2020). Advanced porous graphene materials: From in-plane pore generation to energy storage applications. *Journal of Materials Chemistry A 8*(13), 6125–6143.

(101) Terrones, H., R. Lv, M. Terrones, and M. S. Dresselhaus (2012). The role of defects and doping in 2d graphene sheets and 1d nanoribbons. *Reports on Progress in Physics 75*(6), 062501.

(102) Tian, R., L. Zhao, A. Wu, S. Zhang, G. Zhang, M. Yao, and H. Huang (2023). Atomic-level understanding on progressive lithiation of few-layer mos2 with surface vacancies. *Journal of Alloys and Compounds 939*, 168663.

(103) Tritsaris, G. A., E. Kaxiras, S. Meng, and E. Wang (2013). Adsorption and diffusion of lithium on layered silicon for li-ion storage. *Nano letters 13*(5), 2258–2263.

(104) Uthaisar, C. and V. Barone (2010). Edge effects on the characteristics of li diffusion in graphene. *Nano letters 10*(8), 2838–2842.

(105) Verble, J., T. Wietling, and P. Reed (1972). Rigid-layer lattice vibrations and van der waals bonding in hexagonal mos 2. *Solid State Communications 11*(8), 941–944.

(106) Walsh, E. D., X. Han, S. D. Lacey, J.-W. Kim, J. W. Connell, L. Hu, and Y. Lin (2016). Dry-processed, binder-free holey graphene electrodes for supercapacitors with ultrahigh areal loadings. *ACS Applied Materials & Interfaces 8*(43), 29478–29485.

(107) Wan, L., Z. Ren, H. Wang, G. Wang, X. Tong, S. Gao, and J. Bai (2011). Graphene nanosheets based on controlled exfoliation process for enhanced lithium storage in lithium-ion battery. *Diamond and Related Materials 20*(5-6), 756–761.

(108) Wang, G., X. Shen, J. Yao, and J. Park (2009). Graphene nanosheets for enhanced lithium storage in lithium ion batteries. *Carbon 47*(8), 2049–2053.

(109) Wang, H., Z. Lu, S. Xu, D. Kong, J. J. Cha, G. Zheng, P.-C. Hsu, K. Yan, D. Bradshaw, F. B. Prinz, et al. (2013). Electrochemical tuning of vertically aligned mos2 nanofilms and its application in improving hydrogen evolution reaction. *Proceedings of the National Academy of Sciences 110*(49), 19701–19706.

(110) Wang, L., Z. Xu, W. Wang, and X. Bai (2014). Atomic mechanism of dynamic electrochemical lithiation processes of mos2 nanosheets. *Journal of the American Chemical Society 136*(18), 6693–6697.

(111) Wang, Q. H., K. Kalantar-Zadeh, A. Kis, J. N. Coleman, and M. S. Strano (2012). Electronics and optoelectronics of two-dimensional transition metal dichalcogenides. *Nature nanotechnology 7*(11), 699–712.

(112) Wang, S., C. Li, T. Wang, P. Zhang, A. Li, and J. Gong (2014). Controllable synthesis of nanotube-type graphitic c3n4 and their visible-light photocatalytic and fluorescent properties.

(113) Wang, X., H. Liu, M. Huttula, Y. Luo, M. Zhang, and W. Cao (2019). First-principles studies of lithium adsorption and diffusion on silicene with grain boundaries. *International Journal of Quantum Chemistry 119*(13), e25913.

(114) Wang, X., Y. Luo, T. Yan, W. Cao, and M. Zhang (2017). Strain enhanced lithium adsorption and diffusion on silicene. *Physical Chemistry Chemical Physics 19*(9), 6563–6568.

(115) Wang, Z., Y. Liu, F. Li, and J. Zhao (2021). Controlled 2h/1t phase transition in mos 2 monolayers by a strong interface with m 2 c mxenes: a computational study. *Physical Chemistry Chemical Physics 23*(36), 20107–20116.

(116) Wang, Z. and B. Mi (2017). Environmental applications of 2d molybdenum disulfide (mos2) nanosheets. *Environmental science & technology 51*(15), 8229–8244.

(117) Xiao, J., D. Choi, L. Cosimbescu, P. Koech, J. Liu, and J. P. Lemmon (2010). Exfoliated mos2 nanocomposite as an anode material for lithium ion batteries. *Chemistry of Materials 22*(16), 4522–4524.

(118) Xing, Z., J. Tian, Q. Liu, A. M. Asiri, P. Jiang, and X. Sun (2014). Holey graphene nanosheets: large-scale rapid preparation and their application toward highly-effective water cleaning. *Nanoscale 6*(20), 11659–11663.

(119) Yu, Y., S.-Y. Huang, Y. Li, S. N. Steinmann, W. Yang, and L. Cao (2014). Layer-dependent electrocatalysis of mos2 for hydrogen evolution. *Nano letters 14*(2), 553–558.

(120) Yue, Q., J. Kang, Z. Shao, X. Zhang, S. Chang, G. Wang, S. Qin, and J. Li (2012). Mechanical and electronic properties of monolayer mos2 under elastic strain. *Physics*

Letters A 376(12-13), 1166–1170.

(121) Zeng, Z., K. Li, L. Yan, Y. Dai, H. Guo, M. Huo, and Y. Guo (2014). Fabrication of carbon nitride nanotubes by a simple water-induced morphological transformation process and their efficient visible-light photocatalytic activity. *RSC Advances 4*(103), 59513–59518.

(122) Zhang, W., C.-P. Chuu, J.-K. Huang, C.-H. Chen, M.-L. Tsai, Y.-H. Chang, C.-T. Liang, Y.-Z. Chen, Y.-L. Chueh, J.-H. He, et al. (2014). Ultrahigh-gain photodetectors based on atomically thin graphene-mos2 heterostructures. *Scientific reports 4*(1), 1–8.

(123) Zhao, H., G. Yang, X. Gao, C. H. Pang, S. W. Kingman, and T. Wu (2016). Hg0 capture over comos/γ-al2o3 with mos2 nanosheets at low temperatures. *Environmental science & technology 50*(2), 1056–1064.

(124) Zhao, S., K. Wang, X. Zou, L. Gan, H. Du, C. Xu, F. Kang, W. Duan, and J. Li (2019). Group vb transition metal dichalcogenides for oxygen reduction reaction and strain-enhanced activity governed by p-orbital electrons of chalcogen. *Nano Research 12*, 925–930.

(125) Zhao, T., H. Shu, Z. Shen, H. Hu, J. Wang, and X. Chen (2019). Electrochemical lithiation mechanism of two-dimensional transition-metal dichalcogenide anode materials: intercalation versus conversion reactions. *The Journal of Physical Chemistry C 123*(4), 2139–2146.

(126) Zhou, L.-J., Z. Hou, and L.-M. Wu (2012). First-principles study of lithium adsorption and diffusion on graphene with point defects. *The Journal of Physical Chemistry C 116*(41), 21780–21787.

(127) Zhu, Y., D. K. James, and J. M. Tour (2012). New routes to graphene, graphene oxide and their related applications. *Advanced materials 24*(36), 4924–4955.

(128) Zhu, Y., S. Murali, W. Cai, X. Li, J. W. Suk, J. R. Potts, and R. S. Ruoff (2010). Graphene and graphene oxide: synthesis, properties, and applications. *Advanced materials 22*(35), 3906–3924.

(129) Zhu, Z. Y., Y. C. Cheng, and U. Schwingenschlögl (2011). Giant spin-orbit-induced

spin splitting in two-dimensional transition-metal dichalcogenide semiconductors. *Physical Review B 84*(15), 153402.